UVicSPACE: Research & Learning Repository

University of Victoria

Faculty of Science

Faculty Publications

This is a post-review version of the following article:

Quantifying parental MORB trace element compositions from the eruptive products of realistic magma chambers: parental EPR MORB are depleted

L.A. Coogan, S.E. Dosso

2016

The final published version of this article can be found at:

https://doi.org/10.1093/petrology/egw059

Citation for this paper:

Coogan, L.A. & Dosso, S.E. (2016). Quantifying parental MORB trace element compositions from the eruptive products of realistic magma chambers: parental EPR MORB are depleted. *Journal of Petrology, 57(11-12)*, 2105-2126. https://doi.org/10.1093/petrology/egw059

Quantifying parental MORB trace element compositions from the eruptive products of realistic magma chambers: parental EPR MORB are depleted

COOGAN L.A.[a]* AND DOSSO S.E.[a]

[a]School of Earth and Ocean Sciences, University of Victoria, Victoria, BC, Canada.

*Correspondence to: lacoogan@uvic.ca; tel: (1) 250 472 4018; fax (1) 250 721 6200

Running title: Quantifying parental MORB

ABSTRACT

At fast-spreading mid-ocean ridges the existence of a near steady-state axial magma lens indicates that melt differentiation is an open system process. Field relations in ophiolites and tectonic windows at fast spreading ridges along with some chemical characteristics of mid-ocean ridge basalts (MORB) and oceanic plutonic rocks indicate assimilation is a common process in and around the axial magma lens. Magma and mush zone mixing and mingling is indicated by the petrology of MORB and oceanic plutonic rocks; mush disaggregation provides an efficient mechanism for return of interstitial melt to an eruptible reservoir – a form of in situ *crystallization. Despite such copious evidence to the contrary, MORB differentiation is generally modeled assuming perfect fractional crystallization (Rayleigh distillation). Here we present a simple open system model for MORB differentiation that includes assimilation and* in situ *crystallization that can be used to generate synthetic basalt datasets to compare to natural sample suites. Inversion of the model allows the parental melt compositions to be quantitatively estimated. We use a numerical Bayesian inversion scheme to determine the parental melt compositions for three large (>150 samples in each) normal-MORB suites from the East Pacific Rise. The parental melt compositions determined this way differ significantly from those that would be calculated assuming closed system fractional crystallization. Parental MORB are more depleted than commonly assumed, suggesting either that the upper mantle is more depleted than generally believed and/or that the extent of melting is larger (for example, with melts poorly focused to the ridge axis). The more depleted character of parental than erupted melts has important implications for using basalt trace element systematics*

in chemical geodynamic models. For example, the Sm/Nd of parental MORB are significantly lower than those of erupted MORB and this needs considering in models of the Nd-isotope evolution of the mantle.

Keywords: crystallization modeling; depleted mantle; magma chamber; mid-ocean ridge; MORB

INTRODUCTION

By comparing the composition of melts generated in experiments at different pressures, and in equilibrium with different mineral assemblages, with the composition of erupted basalts, Mike O'Hara (1965) demonstrated that erupted basalts are not "primary". Instead, he suggested a model in which magmas evolve through "*appreciable crystal fractionation*" as they move towards the surface. In particular, he argued that the growth of the olivine stability field with decreasing pressure would lead to substantial amounts of olivine fractionation (perhaps accompanied by pyroxene assimilation; O'Hara, 1968a). Similarly, O'Hara (1968b) showed that the vast majority of Mid-Ocean Ridge Basalts (MORB) are not in equilibrium with orthopyroxene at any pressure despite orthopyroxene being a ubiquitous upper mantle phase. Likewise, he showed that MORB are only in equilibrium with olivine at low pressures (O'Hara, 1968b). Thus, erupted MORB must have evolved via partial crystallization of olivine, with or without other crystallizing phases, after separation from their source. These conclusions, largely drawn from experiments in simple systems, have subsequently been demonstrated to hold in complex natural systems (Fig. 1; e.g. Stolper, 1980; Falloon and Green, 1988; Falloon et al., 1988; Hirose and Kushiro, 1993; Hirose and Kawamura, 1994). Indeed, MORB have major element compositions that are very similar to those of melts that crystallize olivine and plagioclase (troctolite) or olivine, plagioclase and clinopyroxene (gabbro) in experiments at atmospheric pressure (Fig. 1). Further support for MORB major element compositions being controlled by low-pressure crystal-melt separation comes from the occurrence of olivine, plagioclase and more rarely clinopyroxene as the crystal cargo in MORB (e.g. Bryan, 1983), and from the observation that the Mg# of MORB are too low

to be in equilibrium with mantle olivine (Fig. 1). This petrological evidence has led to the widespread acceptance that MORB undergo substantial differentiation in shallow-level magma chambers. Primitive plutonic rocks recovered from the lower oceanic crust provide insight into the crystallization products produced during differentiation but few such samples have been recovered from the ocean basins (e.g. Perk et al., 2007; Gillis et al., 2014). Independent support for extensive low-pressure differentiation of MORB comes from geophysical studies that have imaged a magma lens beneath mid-ocean ridges at fast-spreading ridges near the base of the sheeted dike complex (e.g. Detrick et al., 1987; the so-called axial magma lens or AML). This AML overlies a much larger region of lower crust that contains a mixture of crystals and melt (Dunn et al., 2000; Crawford and Webb, 2002). Since MORB erupted on-axis must pass through the mush zone and AML in transit from the mantle to the surface this further confirms the role of magma chambers in controlling MORB compositions.

Once it is acknowledged that partial crystallization is an important process in controlling MORB major element compositions a key question becomes how does this differentiation affect MORB trace element compositions? An intimately linked question is whether we can use simple approaches to "see through" melt differentiation and identify parental melt trace element characteristics that can be used, for example, in determining mantle temperature, composition and dynamics. For example, average MORB compositions have been used as average oceanic crust compositions in geochemical mass balance modeling which requires the assumption that partial crystallization is inefficient at enriching incompatible elements in MORB (e.g. Hofmann, 1988).

Many studies of the compositional evolution of basalts compare measured compositions to differentiation models that assume perfect fractional crystallization. This approach appears to have become widely accepted because reasonable fits to the general form of major element differentiation trends can be achieved using such models. Based on this it is almost ubiquitously assumed that incompatible element abundances can readily be back-tracked to parental abundances using a fractional crystallization model and that incompatible element ratios are largely unaffected by crustal differentiation processes (although with notable exceptions such as O'Hara, 1977; O'Hara and Mathews, 1981; Defant and Nielsen, 1990; Nielsen and DeLong, 1992; O'Hara and Fry, 1996a, 1996b; O'Neill and Jenner, 2012). In nature differentiation is likely to be far more complex than perfect fractional crystallization. Magma chambers are expected to generally be open systems undergoing replenishment and tapping leading to potentially very different differentiation paths than those followed during closed system fractional crystallization (e.g. O'Hara, 1977; 1980; O'Hara and Mathews, 1981; Albarède, 1985; Defant and Nielsen, 1990). Assimilation of the surrounding country rock is another open system process that has important chemical consequences for magma differentiation (as well a thermal consequences; O'Hara, 1980). Additionally, crystal-melt separation does not have to occur in a single, well-mixed magma reservoir. Instead magmas can differentiate and mix in different parts of the magmatic system, again leading to chemical consequence quite unlike those of simple fractional crystallization (Langmuir, 1989; Nielsen and DeLong, 1992; O'Hara and Fry, 1996a). Overall, the most general conclusion of a wide range of studies of realistic differentiation processes is that it is likely that incompatible elements are substantially more enriched, and compatible

elements substantially less depleted than during an equivalent mass fraction of perfect fractional crystallization (O'Hara, 1977; O'Hara and Mathews, 1981; Albarède, 1985; Langmuir, 1989; Defant and Nielsen, 1990; Nielsen and DeLong, 1992; O'Hara and Fry, 1996a; O'Hara and Fry, 1996b; O'Hara and Herzberg, 2002).

Here we use a realistic magma chamber model to quantify parental MORB compositions. The composition of parental MORB (or equivalently the bulk oceanic crust) provides important constraints on global geochemical models. We start by developing the simplest plausible forward model of differentiation at a fast-spreading ridge that can be used to generate synthetic basalt datasets to compare with natural datasets. We then use a numerical Bayesian inversion approach to estimate the parental melt compositions required to best reproduce three large normal (N-) MORB datasets from the East Pacific Rise (EPR). The resulting parental melts are markedly more depleted than generally expected for N-MORB.

A REALISTIC MAGMA CHAMBER MODEL FOR FAST SPREADING RIDGES

Fast-spreading mid-ocean ridges have near steady-state melt bodies close to the base of the sheeted dike complex and this is underlain (and probably surrounded) by a partially molten mush zone (Detrick et al., 1987; Kent et al., 1993; Dunn et al., 2000; Crawford and Webb, 2002; Carbotte et al., 2013). The small size of the AML (roughly tens of meters high and 500 to 1000 m wide), and the high heat output from the roof of this body into the overlying hydrothermal system, demonstrate that replenishment must occur on a decadal timescale to prevent it freezing (e.g. Liu and Lowell, 2009). Replenishment is also indicated by the petrology and geochemistry of many MORB and their crystal cargo (e.g. Dungan and Rhodes, 1978; Rhodes et al., 1979) and modeling of diffusive exchange

between crystals in MORB and their host basalt suggests that replenishment must commonly immediately precede eruption (Pan and Batiza, 2002; Costa et al., 2009, Moore et al., 2014). Thus, in the model developed below it is assumed that differentiation occurs in a replenished (R) and tapped (T) magma chamber in which tapping occurs after replenishment and mixing (M) and prior to crystallization (X) of the mixed magma (RMTX in the terminology of O'Hara and Herzberg, 2002).

Parental melt replenishing the AML may crystallize prior to mixing with the resident magma, either during transport through the lower crust, if conditions are cool enough, or after replenishing the AML if the more primitive, denser, magma does not immediately mix with the resident magma (e.g. Huppert and Sparks, 1980). Some crystallization of the parental melt prior to mixing with the magma resident in the AML is suggested by the crystal cargo of MORB. Olivine and plagioclase crystals in MORB are commonly too primitive to be in equilibrium with their host (e.g. Coogan and O'Hara, 2015). This observation is consistent with some crystallization of the primitive replenishing melt prior to mixing with a more evolved melt resident in the AML. Thus, in the model developed below it is assumed that the replenishing melt may undergo some (perfect fractional) crystallization of troctolite prior to replenishing the AML (Fig. 2).

Thermal arguments suggest that magma chambers will commonly assimilate their roofs consistent with copious field evidence for assimilation (e.g. O'Hara, 1978; O'Hara, 1980). Compelling evidence for assimilation of the roof of the AML comes from over-enrichment in Cl in some MORB (Michael and Schilling, 1989) and oceanic gabbros (Gillis et al., 2003) as well as in the form of xenoliths of sheeted dikes in the upper

gabbros in ophiolites (e.g. Coogan et al., 2003). Thus, realistic models of MORB differentiation must include assimilation (Fig. 2).

At fast spreading ridges melt is present in the lower crust both in the commonly melt-dominated AML, and in a much larger mush zone below (and around) this body. Crystallization is likely to occur in both the AML and the mush zone with the relative extents of crystallization in each being dependent on the thermal structure of the crust. Crystallization in the AML is likely to be closer to perfect fractional crystallization than to equilibrium crystallization due to the rapid rate of heat extraction into the overlying hydrothermal system and the melt-dominated nature of this body. In contrast, slower cooling and crystallization is expected in the mush zone and crystallization may more closely approach equilibrium crystallization. Return of some fraction of the interstitial melt from the mush zone to the eruptible melt in the AML can occur through numerous processes (compaction, compositional convection, mush zone disaggregation) and will impart the chemical signature of *in situ* crystallization (Langmuir, 1989; Nielsen and DeLong, 1992; O'Hara and Fry, 1996). Mush zone disaggregation associated with replenishment (Fig. 2) is well documented in EPR MORB in the form of cumulate xenoliths and glomerocrysts in lavas (e.g. Hekinian et al., 1985; Ridley et al., 2006; Moore et al., 2014); an elegant model showing this process has recently been reported by Bergantz et al. (2015). We divide crystallization into two zones in the model. Perfect fractional crystallization is modeled for the AML and equilibrium crystallization is modeled for the boundary layer (mush zone). In both regions partition coefficients for a gabbroic mineral assemblage are used. Only a given fraction of the residual melt left after

crystallization in the boundary layer is added back to the AML with some being 'trapped' within the mush zone.

Quantifying a non-steady-state magma chamber model

The magma chamber model described above is perhaps the simplest realistic model of MORB differentiation at fast-spreading ridges (Fig. 2) – many more complications could be imagined. O'Hara (1977, 1980), O'Hara and Mathews, 1981, Albarède (1985, see reformulation in O'Hara and Herzberg, 2002) and O'Hara and Herzberg (2002) quantified the steady state composition of melts erupted from such open system magma chambers using some simplifying approximations. O'Hara's work demonstrated the large differences between the composition of the parental melt and the erupted melt when realistic magma chamber processes are considered. However, the steady state approximation assumes that all controlling parameters are fixed and hence leads to a constant erupted melt composition. A more realistic model of a mid-ocean ridge magma chamber would allow the controlling parameters to vary between cycles generating compositional variability in the model erupted products (as is observed in nature). In this case the model eruptive products depend on both the average value of an input parameter and its variability (tracked here through the standard deviation of the parameter). The model described above (Fig. 2) is straightforward to quantify, relying only on mass balance and the fraction and equilibrium crystallization equations (Appendix A). However, generating a synthetic dataset of MORB compositions, to compare to observed compositions, requires appropriate values, or bounds, for a number of input parameters.

Our approach here is to consider the simplest possibly scenario, that of a constant parental melt composition. While parental melt heterogeneity undoubtedly exists, how

much compositional variability there is in melts feeding the AML is unclear. More importantly, we wish to start simple (and shallow) and test whether magma chamber processes that are known to occur can generate suites of basalt compositions similar to those observed. If they can then models that *a priori* assume that observed compositional heterogeneity is generated in the mantle (while making the demonstrably incorrect assumption that perfect fractional crystallization is the only differentiation mechanism) are, at best, non-unique.

The magma chamber model considered here (Fig. 2) requires values for the average and standard deviation of the following parameters, as well as bounds on the maximum and minimum permitted values (Table 1):

(i) the relative mass fractions of melt in the AML and boundary layer prior to crystallization;

(ii) the mass fractions of melt remaining after crystallization for the parental (replenishing) melt, the melt in the AML and the melt in the boundary layer;

(iii) the mass fractions of the melt remaining in the boundary layer after crystallization that is returned to the magma reservoir;

(iv) the mass fraction of the magma reservoir replenished and tapped; and

(v) the composition and mass fraction of material assimilated.

Additionally, the model requires values for the bulk partition coefficients during troctolite and gabbro crystallization (Table 2). Given these parameters, and a parental melt composition, the model can be used to generate a synthetic dataset.

While it is likely the material assimilated comes either from the base of the sheeted dike complex, or gabbros plated to the roof of the AML, determining the composition of the material added to the magma reservoir is complex. Evidence for assimilation is clearest in the behaviour of Cl that is derived from seawater, indicating earlier hydrothermal alteration of the assimilated material. However, the amount of assimilation is not readily quantified using a basalts Cl content because it is unclear what fraction of the Cl is derived from altered rock (low Cl) versus brine (high Cl). To avoid the assumed Cl content of the assimilated rocks controlling the amount of assimilation required in the modeling presented below, Cl is not considered here. Additionally the extent of alteration of other elements prior to assimilation is difficult to constrain and as a first approximation we ignore all chemical changes due to alteration. Whether material is assimilated en masse or via partial melting may also be important in controlling the composition of assimilated material. Partial melting of the base of the sheeted dikes complex has been documented in ophiolites and oceanic crust based on the occurrence of felsic bodies (e.g. Gillis and Coogan, 2002; France et al., 2009). If such partial melts were extracted from their residue and incorporated into erupted melts the compositional characteristic of the erupted melts would be very different than if bulk assimilation occurs. It is important to recognize that the geological record of the dike-gabbro boundary (or roof of the AML) is likely to preserve the processes operating at the off-axis edges of the AML. Processes operating at the ridge axis have near zero preservation potential in the rock record because repeated cycles of crystallization and assimilation probably occur – bulk assimilation is likely in this setting. Thus, as a first approximation, in the model developed below bulk assimilation of the roof rocks is assumed. Based on

this the composition of the assimilant is taken as the average composition of the last 500 erupted melts (i.e. assuming assimilation of a 500 m wide roof zone and 1 m wide dikes). Because the composition of the material assimilated is taken as the average of the last 500 erupted compositions, and to eliminate any memory of the initial conditions, the first 500 cycles of the model are discarded and the synthetic dataset is generated by running a further 100,000 cycles.

The partition coefficients used in modeling differentiation play a significant role in the results obtained and a complete model will require a fully coupled phase equilibria and trace element model (e.g. Defant and Nielsen, 1990; Nielsen and DeLong, 1992). This is beyond the scope of this work, in part because the computational requirements are non-trivial. It should be noted that the exclusion of a major element model means that fixed mineral modal proportions are assumed in determining bulk partition coefficients – in reality the mode of the crystallizing assemblage will depend on the magma chamber process (e.g. Defant and Nielsen, 1990; Nielsen and DeLong, 1992). For ease of comparison with previous work, and to ensure our choice of partition coefficients is unbiased, we use the partition coefficients for olivine (ol), plagioclase (pl) and clinopyroxene (cpx) compiled by O'Neill and Jenner (2012); exceptions to this are if they do not report a partition coefficient for an element or if this is expected to substantially change during differentiation as documented below. We note that the plagioclase LREE partition coefficients, and especially the plagioclase Eu partition coefficient, in this compilation appear rather low. Partition coefficients for Y, V and Cr are not reported by O'Neill and Jenner (2012). The partition coefficients for Y are assumed to match those given by O'Neill and Jenner (2012) for Er. The partition coefficients for olivine and

clinopyroxene for V and Cr are taken from analyses of phenocryst-matrix pairs from natural MORB (Bougault and Hekinian, 1974) and the partition coefficients of these elements into plagioclase are assumed to be zero. The effect of Cr-spinel crystallization on the chromium partition coefficient during troctolite precipitation is approximated assuming a partition coefficient of 250 and an olivine to spinel ratio of 100 (Roeder et al., 2006); this has the effect of increasing the bulk partition coefficient by 0.75 a value with a significant uncertainty – future work will need to improve upon this approach. The partition coefficients for Sr and Na into plagioclase are expected to change during differentiation. The plagioclase-melt partition coefficient is assumed to be 1.25 during crystallization of troctolite (An_{90}) and 1.55 during crystallization of gabbro (An_{80}) based on the model of Blundy and Wood (1990). The partition coefficient for Na into plagioclase is taken from the output of the Petrolog models presented by Coogan and O'Hara (2015) as 1.0 for troctolite and 1.5 for gabbro (compared to a value of 1.4 used by O'Neill and Jenner, 2015). The bulk partition for MgO is taken as 2.0 for troctolite crystallization and 1.9 for gabbro crystallization based on the analysis of this in Coogan and O'Hara (2015). Bulk partition coefficients for troctolite and gabbro crystal assemblages are determined using modal proportions of 0.30:0.70 (ol:pl) and 0.08:0.52:0.40 (ol:pl:cpx) respectively. As noted above, in reality during open system differentiation these will vary and these fixed values are a simplification (e.g. Defant and Nielsen, 1990).

Some simple model results

The model described above is controlled by the values of the average and standard deviation of eight parameters (Table 1). Given this large number of variables it is

impossible to describe all possible permutations; instead some examples of realistic model results are presented in this section to introduce the variability in erupted melt compositions expected from such a magma chamber. To limit the number of variables to explore in these examples, the ratio of the mass of tapped material less that assimilated, to the mass crystallized or trapped in the boundary layer, is set to one to four in the input parameters (this constraint is relaxed for the inversion as discussed below). This approximates a crust with 20% upper crust and 80% lower crust. When changing other parameters material balance is maintained by shifting the mass fraction crystallized in the AML and/or mass fraction replenished to maintain this upper/lower crust ratio; i.e. although we investigate changes in one controlling parameter at a time below these have to be accompanied by other changes in the system.

Figures 3 and 4 show synthetic datasets for the variation in Th and Cr with differentiation (traced by MgO) generated by varying the average value of one parameter at a time. All standard deviations on the controlling parameters are held constant in all models shown in Figures 3 and 4.

Increasing the average mass fraction of the magma reservoir erupted from 3.5% to 7% (Fig. 3a versus 3b and 4a versus 4b) can be mass balanced by an increase in the extent of crystallization in the AML (to maintain the ratio of upper-to-lower crust) and hence an increase in the mass fraction replenished. The resulting melts produced have similar average MgO and Cr contents but higher, and more variable, incompatible element abundances and high ratios of more-to-less incompatible elements. This is largely due to the greater extent of crystallization driving the incompatible element abundances up with the replenishing melt buffering the compatible element abundances

(c.f. O'Hara, 1977; O'Hara and Mathews, 1981; Albarède, 1985; O'Hara and Herzberg, 2002).

Partitioning more of the melt in the magma reservoir into the boundary layer leads to an overall decrease in the total extent of crystal fractionation (which is accounted for by a decrease in the mass fraction crystallization in the AML in Figs. 3d and 4d relative to 3c and 4c), because some of the melt in the boundary layer is assumed to freeze in place forming lower crust with no crystal-melt separation. In this model erupted melts have higher average compatible element abundances and lower incompatible element abundances and have lower ratios of more-to-less incompatible elements. This is perhaps somewhat counter-intuitive as this process can be thought of as involving a larger fraction of *in situ* crystallization; the result is controlled by the requirement to produce the same upper-to-lower crust mass ratio in all models and that more of the lower crust is comprised of frozen melt in models with more melt partitioned into the boundary layer, all other things being equal.

Increasing the extent of crystallization within the boundary layer (from 5% to 25% in Figs. 3e, 3f, 4e and 4f) leads to a decrease in the extent of crystallization in the AML to maintain the same relative masses of upper and lower crust, with no change in the mass fraction replenished. If more of the crystallization occurs in the boundary layer the average erupted melts have higher MgO and Cr but also have higher, and more variable, incompatible element abundances at a given MgO content (c.f. Langmuir, 1989; O'Hara and Fry, 1996). This reflects both the fact that equilibrium crystallization is assumed to occur in the boundary layer, and that the smaller extent of crystallization in

the AML leads to less depletion of compatible elements in the resulting melts than when this body crystallizes to a greater extent.

Increasing the fraction of the melt that remains after crystallization in the boundary layer that is returned to the AML leads to an increase in the extent of crystallization required in the AML to maintain a constant ratio of upper to lower crust (because melt that is not returned from the boundary layer becomes part of the mass of the lower crust). For the smallest possible mass fraction returned, given the other model parameters used, of 81% there is no crystallization in the AML and the resulting melts are MgO-rich and show only moderate incompatible element enrichments relative to fractional crystallization (Fig. 3g). In contrast, if most of the melt remaining after crystallization in the boundary layer is returned to the AML there is a strong enrichment in incompatible elements (Fig. 3h). Compatible element abundances are more depleted in this scenario but are still substantially higher than expected from fractional crystallization (Fig. 4g and 4h).

In summary, the diversity of melt compositions produced in the models shown in Figures 3 and 4, from realistic ranges in the controlling parameters, is substantially larger than would generally be considered to be realistic for derivation from a single parental melt. For example, the erupted melts would have 2 to 4x higher incompatible element abundances than the parental melt composition at an MgO content of 7 wt%. Likewise, incompatible element ratios can vary significantly (e.g. Nb/Y from 1.1 to 1.8x that of the parental melt in the models shown). Despite these large changes in incompatible element abundances and ratios, the Cr content of the melts are not massively depleted, generally being ~50% of that of the parental melt at an MgO content of 6.5 wt%. Clearly the

compositional evolution of the melts erupted from a magma reservoir, such as that shown in Figure 2, are not well approximated by a fractional crystallization model (green line in Figures 3 and 4). Hence, back calculating a parental melt compositions from an observed basalt composition by assuming fractional crystallization is likely to lead to large overestimates of parental melt incompatible element abundances (and potential mantle compositions).

INVERTING THE MODEL

If a suite of lava compositions is generated from a fixed parental melt composition, through a given differentiation process, the compositions contain information about both the parental melt composition and differentiation process. Early attempts to invert this problem, and determine parental melt compositions from lava suites, assumed perfect fractional crystallization (Allegre et al., 1977; Minster et al., 1977). These studies linearized the problem and found best-fitting parental melt compositions given the data. We build on this general concept but with three important differences. First, it is now abundantly clear that fractional crystallization is not the only differentiation process operating in most magmatic systems and we consider differentiation in the magmatic system described above (Fig. 2). Second, there is much information about the differentiation process recorded in the distribution of lava compositions and we utilize this. For example, whether a MORB sample suite has a high or low average MgO content and whether an element has a large or small variability at a given extent of differentiation (e.g. Figs. 3 and 4) carries important information. Based on this we invert for the distribution of data not just average abundances. Finally, we use an advanced non-linear

numerical inversion that allows us to invert the full differentiation model and to quantify the uncertainties on the model parameters as probability densities.

To invert the model to determine the probability densities for the unknown model parameters, and in particular the parental melt composition, we require a method to compare the natural and synthetic datasets. To do this we compare the following summary statistics: (i) the fraction of the dataset that falls within each 0.5 wt% MgO bin (Fig. 5) and (ii) the average and standard deviation of the abundance of each element in each 0.5 wt% MgO bin that has ≥5 data within the bin (Fig. 5).

To invert the model and determine probability densities for the model parameters we also require estimates of the uncertainties for each of the data being inverted for (i.e. the summary statistics). These are not straightforward to determine. However, it is clear that how well defined any of the summary statistics are is largely a function of the number of natural samples that have been used to define the statistic. For instance, if we had a very large number of analyses of natural basalts the data being inverted (the statistics of the large dataset) would have very small uncertainties associated with them. Based on this line of reasoning, the uncertainty on each statistic is calculated using analytical solutions for the uncertainties assuming these are controlled entirely by the sample size (Appendix B).

The elements used in the inversion (Table 2) were selected so as to span a broad range of partition coefficients (and hence behaviour), be relatively immobile during alteration, and be analysed in the majority of the samples in the datasets considered. It should be noted that using multiple elements with similar partition coefficients (e.g. all the heavy rare earth elements) would tend to weight the inversion towards fitting these

data and these do not provide independent constraints. Because of this, elements were selected so as to have a roughly even distribution of partition coefficients in logarithmic space (Table 2).

The range of possible values for any of the model parameters (e.g. mass fractions erupted, crystallized or assimilation) is defined by bounds on the model search space. Realistic bounds on the mass fractions involved in different magma chamber processes can be derived from geological, petrological, geophysical and thermal constraints; however, to ensure that these constraints do not drive the model inversion (see below) broad bounds were place on all parameters (Table 1). The variability, defined using a standard deviation, as well as the average value of each parameter within a given model run is also important to the model results. Again, a broad range of possible values for the standard deviations are searched over to ensure that the bounds on these do not control the result (Table 1). Likewise the range of potential parental melt compositions in the modeling is kept broad to ensure the search space does not control the result and this is confirmed *a posteriori*. The mass fractions erupted, assimilated, crystallized and trapped in the boundary layer define the ratio of upper (lavas and dikes) to lower (plutonic rocks) crust produced by any model. In the inversion the upper crust is constrained to be between 12.5 and 50% of the entire crust.

To solve the inverse problem of estimating the model parameters and their uncertainties from the measured data, a nonlinear Bayesian inference approach was applied. In this approach the parameters are considered random variables constrained by the data and by the parameters bounds (which define a bounded uniform prior probability density). The goal is to estimate statistical properties of the multi-dimensional posterior

probability density (PPD), which accounts for both data and prior information, by drawing samples numerically from the PPD. In particular, the PPD was sampled using the Markov-chain Monte Carlo method of Metropolis–Hastings sampling (e.g. Gilks et al., 1996), in which random parameter perturbations are proposed and then accepted or rejected according to a probabilistic condition (the Metropolis–Hastings criterion). For efficiency, parameter perturbations were applied in a principal-component (rotated) parameter space drawn from a linearized approximation to the PPD (Dosso and Wilmut, 2008). To ensure a sufficiently wide search of parameter space, multiple interacting Markov chains were run within a parallel-tempering formulation (Earl and Deem, 2005; Dosso et al., 2012). This provides both broad sampling of the parameter space and efficient concentrated sampling of the high probability regions. At convergence, the resultant sample of models can be interpreted in terms of PPD properties such as marginal probability densities (one-dimensional probability densities for individual parameters, with the effects of all other parameters averaged out), or the maximum *a posteriori* (MAP) model which maximizes the PPD and is hence the most-probable parameter set.

Testing the inversion approach with synthetic data

To test the inversion approach we generated synthetic datasets using the forward model with the same number of data as the natural datasets and ran the inversion for these. Effectively, this tests how much information datasets of these sizes (number of samples and number of elements) carry about the parental melt composition and model parameters. Because synthetic data were generated using the forward model the true model parameters are all known. The results for one such inversion are shown in

Appendix C and just a few salient features noted here. Firstly, and most importantly here, the parental melt composition is quite well recovered with the true parental melt composition lying within the region of high probability models (for example, in the model shown the parental melt contained 0.62 wt% TiO_2 and the MAP solution was 0.67 wt%). For some synthetic data inversions we performed the peak in the marginal probability densities for the more incompatible elements, and the MAP model, were offset to somewhat higher abundances than the true parental melt. Whether this is an inherent feature of the modeling approach, or a feature of the model parameters used for those specific inversions, is unclear (a single inversion can take a week to run limiting the number of such runs that is plausible). Some of the magma reservoir model parameters are recovered well by the inversion and others less so. The average values of most parameters are recovered well except the average mass fractions erupted and assimilated which, to some extent, can play-off against one another; the synthetic datasets provide little information about these parameters. The inversion does not constrain the standard deviation of the mass fractions erupted, assimilated, partitioning into the boundary layer or trapped in the boundary layer. The standard deviations are somewhat better constrained by the inversion for: (i) the mass fraction of melt remaining in the AML after crystallization; (ii) the mass fraction of melt remaining in the boundary layer after crystallization; (iii) the mass fraction of replenishing melt; and (iv) how much the replenishing melt crystallizes prior to mixing into the AML. Another inversion of synthetic data, except with twice as many data as in the natural datasets, showed that doubling the number of data leads to little improvement in how well the model parameters can be extracted from the data.

Three EPR MORB datasets used in the inverse modeling

Below we model differentiation of three spatially restricted EPR MORB datasets to determine the parental melt composition and magma chamber parameters. Here these datasets are introduced and some salient features of their differentiation trends noted. For the modeling approach described above to work well several criteria must be fulfilled: (i) the natural dataset must contain sufficient samples that it can be described meaningfully using the summary statistics; (ii) the natural dataset must have been analysed for a sufficiently broad range of elements that different differentiation processes can be identified; and (iii) ideally there would be no *a priori* evidence that the natural samples were generated by the differentiation of more than one parental melt composition. Applying the latter criterion has the potential to become circular however, as what compositional variations are generated by differentiation versus partial melting is controversial.

The three datasets modeled below come from: (i) 9.6-10°N on the EPR (hereafter 9°N; dataset submitted to PetDB by Mike Perfit in 2013, cf. Perfit et al., 1994; Perfit et al., 2012); (ii) the Hess Deep tectonic window (formed at ~2°N on the EPR and exposed due to Cocos Nazca rifting; Stewart et al., 2002); and (iii) the Pito Deep tectonic window (formed at ~23°S on the EPR and exposed due to microplate rotation; Pollock et al., 2009). Each contains >150 samples, analyzed for a broad suite of trace elements, from a spatially restricted area. The 9°N dataset represents a near instantaneous sampling along (and a few kilometers across) the ridge axis and the latter two are timeline sample suites representing <0.5 Myr of magma compositions from the same geographical region of the EPR. Additionally, the latter two are dominated by dike samples which allow a greater

range of melts tapped from the AML to be determined in a small area than using just surficial samples of lavas which generally only recover the last flow in a given area. The 9°N dataset represents the northern portion of the well-studied 9-10°N segment; samples from south of 9.6°N are not considered here as they show heterogeneous radiogenic isotope compositions inconsistent with generation via the differentiation model used here. The tectonic window datasets suffer from uncertainties about element mobility during hydrothermal alteration, as these include both lavas and dikes; unfortunately, this cannot be avoided given currently available data.

The three basalt suites show subtle difference in major element compositions (Fig. 1c-e) including different distributions of their extent of differentiation, as tracked by the distribution of MgO contents (Fig. 6a). The 9°N sample suite is the most primitive, averaging ~1 wt% higher MgO contents than the Hess Deep samples, with the Pito Deep samples intermediate between these. In addition to the average MgO content the datasets show somewhat different distributions of MgO with the Pito Deep sample suite most evenly distributed and the Hess Deep dataset showing the sharpest peak in MgO content. Since the MgO content of a basalt is strongly correlated to its liquidus temperature, these differences presumably reflect difference in the thermal state of the magma reservoir immediately prior to eruption. Overall, the 9°N dataset shows the least variability in major element compositions (Fig. 1c-e).

In terms of the highly compatible elements, Cr and Ni, all three sample suites show a similar decrease in their abundance with decreasing MgO as expected (Fig. 6b). In detail, the Pito Deep samples generally have slightly lower Cr contents, at a given MgO content, than the 9°N and Hess Deep samples at least in the more evolved samples.

All sample suites have large variations in compatible element abundance at a given MgO content (Fig. 6b). This is inconsistent with closed system fractional crystallization of a single parental melt composition, which would generate no variability in any element abundance at a given MgO content. All datasets also show an increase in the relative variation of the compatible elements, defined by the relative standard deviation in a 0.5 wt% MgO interval, with decreasing MgO. This is weakly defined for Ni but more strongly defined for Cr (Fig. 6b inset); this increased variability of compatible element abundances with decreasing MgO is difficult to explain by mixing of different parental melt compositions (Shorttle, 2015) and most likely reflects differentiation induced heterogeneity.

The three sample suites are all relatively typical N-MORB except a single incompatible element enriched sample in the Pito Deep suite. This sample is much more enriched in incompatible elements than any other from this (or the other) sample suites (Pollock et al., 2009). For example, it has a La_n/Yb_n (subscript n = chondrite normalised) ratio of 5.05 while the remaining Pito Deep samples have an average of 0.56±0.10 (1σ). This sample is clearly anomalous, most likely having a different parental melt composition and bypassing the axial magma plumbing system, and is excluded from all further discussion and modeling. The Hess Deep (average La_n/Yb_n = 0.67±0.12) and 9°N (average La_n/Yb_n = 0.77±0.20) sample suites are, on average, slightly less depleted than the Pito Deep sample suite. Likewise, at a given MgO content, the average incompatible element abundances increase in the same order, being the lowest at Pito Deep and the highest at 9°N. Incompatible element abundances in all three sample suites show the well-known "over-enrichment" with decreasing MgO (Fig. 6c) commonly observed in

MORB (Bryan et al., 1976; Bryan and Moore, 1977; Perfit et al., 1983; Hekinian and Walker, 1987; Stewart et al., 2002; O'Neill and Jenner, 2012); i.e. the enrichment of incompatible elements with decreasing MgO content is far greater than can be explained by fractional crystallization (Fig. 6c). Additionally, all locations show significant variability in incompatible element abundances at a given MgO content, again inconsistent with fractional crystallization of a single parental melt composition (Fig. 6c). This has led previous workers to suggest that there must have been variable parental melts feeding the crust in all areas (Stewart et al., 2002; Pollock et al., 2009; Perfit et al., 2012). Whether these variations require differences in parental melt composition, or simply a more complex (realistic) model of magma differentiation than close system fractional crystallization is explored below.

RESULTS: PARENTAL MORB COMPOSITIONS

The inversion results for the parameters that control the differentiation process (Fig. 2, Table 1) show that some of these are not well constrained by the data (Fig. 7); i.e. the probability densities of the parameter values are broad and in some cases almost flat, meaning that models that use a wide range of values can fit the data similarly. This is especially true for the standard deviations on the parameters that in many cases are almost flat indicating that they are unconstrained by the data (Fig. 7). This is not surprising given that the same is true for synthetic datasets generated using the forward model; this indicates that the data do not carry much information about these parameters (Appendix C). Additionally, each dataset gives somewhat different results with the Pito Deep and Hess Deep datasets fit by more similar model parameters than the 9°N dataset.

Despite many of the controlling processes being poorly constrained by the data the parental melt compositions are remarkably tightly constrained, especially for the Pito Deep and 9°N datasets. These results are shown as both probability densities and maximum *a posteriori* values in Figure 8. The former allows the range of probable parental melt compositions to be visualized and the latter shows the most-probable parental melt compositions. The MAP parental melt compositions correspond well to the parental melt probability density maxima for the Pito Deep and 9°N datasets but is offset to a lower value for the highly incompatible elements in the Hess Deep dataset (Fig 8). Both the broader marginal probability densities for the parental melt composition, and the offset of the MAP solution from the peak of the marginal densities, suggest caution is required when interpreting the Hess Deep parental melt composition. That said, there is no reason why the MAP solution should lie at the peak of the marginal probability densities for a non-linear inverse problem, and it frequently does not in other applications. Comparisons of synthetic datasets, generated using the MAP parameters, with the natural sample data for each area are shown in Appendix D so the reader can evaluate visually how well the models reproduce the data. The highly incompatible elements (e.g. Nb) are somewhat less well reproduced by the model for the 9°N dataset perhaps indicating that there was more parental melt heterogeneity in this area.

Two features of the parental melt compatible element compositions are noteworthy. First, the model parental melt MgO contents differ somewhat (10.8-12.9 wt% MgO) and these correlate positively with the model parental melt Ni contents (160-300 ppm). These differences can be explained by 0-5% fractional crystallization of olivine from a melt in equilibrium with mantle olivine prior to the melt co-saturating with

plagioclase (which is the starting point of the inversion). Second, the parental MORB compositions determined here have positive Sr anomalies (Fig. 8). This characteristic has been noted previous for primitive MORB by Niu and O'Hara (2009) and is present in many of the more primitive MORB glasses reported by Jenner and O'Neill (2012) and in many primitive melt inclusions in MORB (e.g. Danyushevsky et al., 2003; Danyushevsky et al., 2004; Laubier et al., 2012).

The most striking feature of the parental melt compositions (Fig. 9) is that they are substantially more depleted in incompatible elements than either: (i) the parental melt composition that would be calculated if simple fractional crystallization was assumed to control differentiation (e.g. fractional crystallization models using the calculated parental melt composition as a starting point substantially underestimate the abundance of highly incompatible elements at any given MgO content; Appendix D); or (ii) commonly used estimates of parental MORB (Fig. 9). When interpreting the parental melt compositions it is important to remember that the modeling approach used here assumes a single parental melt composition. However, many studies suggest parental melt heterogeneity exists in the Moho-crossing melt with mixing and crystallization occurring synchronously in mid-ocean ridge plumbing systems (e.g. Sobolov and Shimizu, 1993; Nielsen et al, 1995; Coogan et al., 2002; Shortle, 2015). If this was the case for the sample suites studied then the parental melt compositions determined here are best thought of as "average parental melt compositions" (although in detail this depends on the mixing and crystallization processes). Clearly, if there was parental melt heterogeneity then the depleted end-member would have to be more depleted than the average parental melt composition determined here.

Perhaps the most widely used depleted MORB mantle (DMM) composition is that of Workman and Hart (2005). They calculate a parental MORB from their estimated DMM using an extent of melting (6%) that is constrained by fitting an unpublished estimate of parental MORB from Su and Langmuir. In comparison to this, and other similar (Hofmann, 1988; Sun and McDonough, 1989; Salters and Stracke, 2004) estimates of parental N-MORB compositions, the parental melt compositions determined here are substantially more depleted (Fig. 9). Of course, if a larger extent of melting had been assumed by Workman and Hart (2005) their parental MORB would also have been more depleted. A more depleted parental MORB composition than generally assumed is supported by a number of lines of reasoning. Firstly, the depleted parental melt compositions determined here overlap with the compositions of the four most primitive (MgO >9.5 wt%) EPR basalts in the compilation of Gale et al. (2013; Fig. 9). Secondly, they overlap with the Ti content of those basalts in the primitive MORB compilation of Presnall and Hoover (1987) with >9.5 wt% MgO (average 0.78 wt% TiO_2). Finally, our parental melt compositions overlap with the model parental MORB calculated by Niu and O'Hara (2009) using an entirely different approach based largely on regression of depleted MORB against MgO back to a putative parental MgO content. Thus, while there is significant variability in the most incompatible element abundances it seems likely that *average* parental MORB, away from enriched regions (i.e. parental N-MORB), lies within the range of parental compositions determined here (Fig. 9). This may have substantial implications for chemical geodynamics.

Taking the Workman and Hart (2005) parental N-MORB as an example of a "standard" view of a parental MORB composition, the more depleted parental melt

suggested here can be explained in at least two ways (assuming a homogeneous mantle source). First, the MORB source may be more depleted than that determined by Workman and Hart (2005; see below). For this model to be correct the depletion would have to be relatively young to avoid development of more depleted radiogenic isotope ratios. Complete analysis of this is beyond the scope of this contribution. Second, the extent of melting beneath the EPR could be larger than suggested by Workman and Hart (2005) leading to a more depleted average melt composition. If parental MORB are generated by 15-20% melting (instead of ~6% as suggested by Workman and Hart, 2005) then our parental melt composition could be generated from the Workman and Hart (2005) DMM composition. To avoid producing overly thick oceanic crust in this model either significant melting would have to start at shallow depth, and have high productivity, or melt focusing to the axis would have to be relatively inefficient.

DISCUSSION

Magmatic differentiation has generally been thought to be incapable of generating large variations in incompatible element abundances and ratios in relatively primitive lavas. One of the more powerful tools available to understand this is the use of elements that change their compatibility substantially between mantle melting and crustal differentiation as exemplified by the "plagiophile" elements (K, Sr, Ba and Eu). We consider the behaviour of these elements first. We then briefly consider one example of the wide-ranging implications of parental MORB melts being more depleted than generally assumed.

Plagioclase and the behaviour of K, Sr, Ba and Eu

Those elements that have significantly higher partition coefficients for plagioclase than any mantle mineral potentially provide useful insight into what proportion of the chemical variability in MORB is derived from the mantle versus crust. O'Neill and Jenner (2012) showed that in their basalt dataset the behaviour of Sr and Eu is different from that of elements with similar incompatibility during mantle melting (e.g. Pr and Eu* = $(Sm \times Gd)^{0.5}$ respectively). They used this to argue that crustal processes play a dominant role in controlling the behaviour of the trace elements in MORB. In contrast, Hofmann (2012) questioned the interpretation of O'Neill and Jenner (2012) based on Ba and K behaving more similarly to elements of the same incompatibility in the mantle rather than in the crust in the same dataset.

The magma chamber model used here leads to far less variability in Sr contents of synthetic lavas than is observed (Fig. 10a-c), suggesting that the model does not capture all of the processes operating in nature. Two general types of models could explain the larger variability in Sr in the data than the model. Firstly, there could be variability in the Sr content of the parental magma, which would have to be accompanied by variability in the abundance of other elements. Alternatively, a crustal process that is not included in the model used here could lead to variability in the Sr content of erupted magmas. These models are not mutually exclusive but they are considered separately as end-members.

During mantle melting Sr and Pr have similar bulk partition coefficients and if melting was the only control on the Sr and Pr abundances they would correlate strongly with one another. This is not the case in the three datasets considered here and, notably, Pr correlates strongly with MgO while Sr does not (Fig. 10). The strong correlation of Pr

with MgO indicates an important role for differentiation in the crustal magma reservoir in controlling the Pr abundance. Importantly, the scatter in Pr content of the samples at a given MgO content does not correlate strongly with their Sr content except in the 9°N data (Fig. 10d-f). This suggests that the scatter in Pr at a given MgO content and the variation in Sr contents do not come from a single source (at least for the Pito and Hess Deep sample suites). For example, if parental melts had correlated variations in Pr and Sr (as expected for simple melting processes), and the observed variation in Sr came from this parental melt heterogeneity, then this would lead to a correlation of Pr and Sr at any given MgO content for a simple differentiation process.

Another important observation with regard to the plagiophile elements is that the Sr and Ba contents correlate in the basalt suites studied here, at least for the Hess and Pito Deep samples (Fig. 10j-l). This is perhaps surprising given that their Sr and Pr abundances do not correlate despite the more similar partition coefficients of Sr and Pr than Sr and Ba during melting. However, if the variability in parental melt Ba was much larger than the variability of Pr (and Sr), differentiation within the magma reservoir would be more significant in controlling the observed variability in Pr than Ba. In contrast, the near unity partition coefficient for Sr in the crust would leave mantle-derived variability as the major control on Sr variability and this could correlate with Ba but not Pr. However, in this model the variation in Ba at a given Sr content would be due to differentiation, and should correlate with the sample MgO content; this is not the case (Fig. 10j-l). Also, if the correlation between Sr and Ba reflected parental melt variability then the Ba and Nb concentrations would be expected to correlate as these are both highly incompatible elements during mantle melting. However, in both the Hess Deep

and Pito Deep datasets Nb correlates less well with Ba than Sr does and much of the range in Ba is observed at a constant Nb content (Fig. 10m-o). The 9°N dataset differs in showing a very strongly correlated covariation of Nb and Ba. This observation, along with Pr correlating with Sr, at a given MgO content, for just the 9°N dataset (Fig. 10f), suggests that the controls on the lava compositions may be somewhat different in this area; perhaps variability in parental melt composition was more important. This suggestion is consistent with the major element variability discussed below.

The major element compositions of the basalts also provide insight into both why the natural samples show greater variability in Sr than predicted by our magma reservoir model (Fig. 10a-c) and the origin of the correlation of Sr and Ba in the natural samples (Fig. 10j-l). There is a striking separation of the high- and low-Ba samples from Hess Deep and Pito Deep (but less clearly in the 9°N data) in terms of the covariation of Al and Fe with MgO (Fig. 11). The same is also true, to a lesser extent, for Si and Ca. This major element variability occurs in samples that contain 6 to 8 wt% MgO; at these MgO contents the basalt are multiply saturated and their major element compositions are largely controlled by low-pressure phase equilibria. The high Ba samples have high Al and low Fe at a given MgO content compared to the low Ba samples, and they also have a tendency to be high in Ca. The same characteristics are present in the East Pacific Rise basalt compilation of Gale et al. (2013) indicating this is not something unique to the Hess and Pito Deep datasets (Fig. 11). The Si contents of the high Ba samples also appear to differentiate them from the other samples albeit in different ways in different sample suites. Stewart et al. (2003) suggested that the low Fe, high Al Hess Deep lavas represented rocks that had accumulated plagioclase, but this cannot explain their being

enriched in Ba relative to other lavas; instead plagioclase addition would act to dilute, and hence reduce, the Ba content of a basalt. One possible explanation for these characteristics is assimilation of hydrothermally altered wall rocks (upper gabbros and lowermost dikes). Addition of water and partial melting of the assimilated material (rather than the bulk assimilation assumed in the model used here) would tend to destabilize plagioclase leading to higher Al contents of plagioclase-saturated melts. Breakdown of plagioclase in the assimilated material could lead to preferential addition of Ba and Sr to the magma at least qualitatively consistent with the enrichment of these elements provided this was accompanied by crystallization of other low Ba phases. Kirchner and Gillis (2012) report an average plagioclase Ba content in the upper Hess Deep gabbros of 9±8 (1σ) ppm compared to an estimated parental melt Ba content of ~2 ppm. This suggests that plagioclase that crystallizes from evolved melts contains sufficient Ba that its assimilation would lead to enrichment in Ba in the result melt. A model of plagioclase dissolution has been used to qualitatively explain positive Ba and Sr anomalies in some Mid-Atlantic Ridge MORB (Laubier et al., 2012). In this model the low Fe content of the high Ba samples from Hess Deep and Pito Deep could be explained by assimilation leading to oxidation of the magma driving FeTi-oxide saturation. It is beyond the scope of this study to fully evaluate the origin of the major element differences that go along with variations in Ba and Sr; we simply conclude that a crustal origin of the excess variability in Sr (Fig. 10), correlated Sr-Ba content and different major element compositions of high-Ba and low-Ba samples (Fig. 11) is at least as plausible as a mantle origin and deserves further investigation.

Sm/Nd in parental versus erupted MORB and implications for estimating DMM

Knowledge of the Sm/Nd of the DMM is critical to using $^{143}Nd/^{144}Nd$ and $^{142}Nd/^{144}Nd$ to understand the chemical evolution of the mantle (e.g. Jackson and Carlson, 2012). Likewise, the widely used DMM compositional model of Workman and Hart (2005) was derived based on a chondritic $^{143}Nd/^{144}Nd$ mantle depletion model that is difficult to reconcile with the non-chondritic $^{142}Nd/^{144}Nd$ of the upper mantle. Because most of their DMM composition model is derived from their estimated Sm/Nd of DMM (0.41), that they determined from this depletion model, uncertainty in this ratio has wide ranging implications. In contrast to the quite depleted Sm/Nd of the MORB source derived by Workman and Hart (2005), Gale et al. (2013) suggest that DMM has a more enriched Sm/Nd of <0.34. Clearly there is a significant uncertainty in the Sm/Nd of DMM, and parental MORB, that needs resolving.

Our inversion provides a new approach to determining the Sm/Nd of parental MORB from observed basalt compositions; such parental MORB compositions can then be used with a melting model to constrain the same ratio in DMM. Coogan and O'Hara (2015) suggested that differentiation of MORB could substantially change the Sm/Nd of erupted MORB compared to the parental melt. They used two different sets of partition coefficients for Sm and Nd during crystallization to evaluate the plausible range of change of Sm/Nd during differentiation. Using the more extreme partition coefficients that Coogan and O'Hara (2015) considered (bulk partition coefficients of Nd and Sm of 0.118 and 0.179 respectively) the MAP differentiation models described above lead to the erupted melt having a Sm/Nd between 4% (9°N) and 18% (Hess Deep) lower than the parental melt. Using the minimum difference in partition coefficients that Coogan and

O'Hara (2015) considered (bulk partition coefficients of Nd and Sm of 0.14 and 0.16 respectively) the MAP differentiation models lead to the erupted melt having a Sm/Nd between 1.5% (9°N) and 6.5% (Hess Deep) lower than the parental melt. As discussed by Coogan and O'Hara (2015) the higher Sm/Nd of parental MORB than erupted MORB is consistent with existing data for the Sm/Nd of spatially associated oceanic plutonics and MORB in which the plutonic rocks have higher Sm/Nd (Coogan, 2014). Thus, it is clear that the Sm/Nd of erupted MORB does not provide a reliable estimate of the Sm/Nd of the average melt generated in the mantle.

SUMMARY AND CONCLUSIONS

Mike O'Hara made "a plea for greater subtlety in the interpretation of trace element and isotope data for basaltic rocks" (O'Hara and Herzberg, 2002). As a step towards answering this plea, we have developed a numerical forward model of the simplest plausible magma reservoir beneath a fast-spreading ridge and used this to generated synthetic basalt datasets to compare to natural datasets. The results reiterate what has been known from simplified analytical models for decades, that realistic magma chamber models lead to quite variable eruptive products that can differ dramatically from the parental melt (Figs. 3 and 4 and Appendix D).

We used the forward model in a numerical inversion scheme to quantify the parental melt composition for three N-MORB suites from the EPR. The results show that parental MORB are more depleted than generally thought (Fig. 9). Fitting a closed system fractional crystallization model through the data would lead to a substantial over estimation of the incompatible element abundances in the parental melt.

The results presented here should be considered a first step towards robust quantification of the composition of parental N-MORB. As Mike O'Hara noted long ago, the phase equilibria of the system needs to be considered in differentiation models (e.g. O'Hara, 1980). Only by coupling a phase equilibria model (e.g. Defant and Nielsen, 1990; Nielsen and DeLong, 1992) to the kind of trace element model presented here can features such as changes in bulk partition coefficients with changing crystallizing phases, and phase proportions, be tracked. This will be especially important for tracking changes in crystallizing modal proportions and for better quantification of the behaviour of some trace elements with complex behaviour (e.g. Cr). Furthermore, there is no doubt that Moho crossing melts have some compositional variability and quantification of this is needed. However, the general conclusion, that parental N-MORB are more depleted than has generally hitherto been appreciated, appears robust. The approaches and general conclusions, of this study are likely to be equally applicable to other types of MORB (e.g. enriched MORB) as well as magmas erupted in other geological environments.

ACKNOWLEDGEMENTS

We thank Yaoling Niu, and his co-conveners, for the invitation to present in the O'Hara session at Goldschmidt 2015 that motivated the completion of this study. We also thank journal reviewers John Sinton, Hugh O'Neill and Roger Nielsen for thought provoking reviews that led to improvements in the manuscript. LAC thanks Mike for his generosity of time, ideas and Mathematica notebooks over the last two decades and for his insistence that simpler isn't always closer to the truth.

REFERENCES

Albarède, F. (1985). Regime and trace-element evolution of open magma chambers. *Nature*. **318**, 356–358.

Allegre, C. J., Treuil, M., Minster, J.-F., Minster, B. & Albarède, F. (1977). Systematic use of Trace Elements in Igneous Process Part I: Fractional Crystallisation Processes in Volcanic Suites. *Contributions to Mineralogy and Petrology* **60**, 57–75.

Bergantz, G. W., Schleicher, J. M. & Burgisser, A. (2015). Open-system dynamics and mixing in magma mushes. *Nature Geosciences* **8**, 793–796.

Blundy, J. D. & Wood, B. J. (1991). Crystal chemical controls on partitioning of Sr and Ba between plagioclase feldspar, silicate melts, and hydrothermal solutions. *Geochimica et Cosmochimica Acta* **55**, 193–209.

Bougault, H. & Hekinian, R. (1974). Rift valley in the Atlantic ocean near 36°50'N - Petrology and geochemistry of basaltic rocks. *Earth and Planetary Science Letters* **24**, 249–261.

Bryan, W. B. (1976). Inferred geologic settings and differentiation in basalts from the deep-sea drilling project. *Journal of Geophysical Research* **81**, 4285–4304.

Bryan, W. B. (1983). Systematics of modal phenocryst assemblages in submarine basalts: petrological implications. *Contributions to Mineral Petrology* **83**, 62–74.

Bryan, W. B. & Moore, J. G. (1977). Compositional variations of young basalts in the Mid-Atlantic Ridge rift valley near lat 36°49'N. *Geological Society of America Bulletin* **88**, 556–570.

Carbotte, S. M., Marjanovic, M., Carton, H., Mutter, J. C., Canales, J. P., Nedimovic, M. R., Han, S. & Perfit, M. R. (2013). Fine-scale segmentation of the crustal magma reservoir beneath the East Pacific Rise. *Nature Geoscience* **6**, 866–870.

Coogan, L. A. (2014). The lower oceanic crust. *Treatise on Geochemistry*, 497–541.

Coogan, L. A., Banks, G. J., Gillis, K. M., MacLeod, C. J. & Pearce, J. A. (2002). Hidden melting signatures recorded in the Troodos ophiolite plutonic suite: evidence for widespread generation of depleted melts and intra-crustal melt aggregation. *Contributions to Mineral Petrology* DOI 10.1007/s00410–002–0413–2.

Coogan, L. A., Mitchell, N. C. & O'Hara, M. J. (2003). Roof assimilation at fast-spreading ridges: an investigation combining geophysical, geochemical and field evidence. *Journal of Geophysical Research* **108**, DOI 10.1029/2001JB001171.

Coogan, L. A. & O'Hara, M. J. (2015). MORB differentiation: In situ crystallization in replenished-tapped magma chambers. *Geochimica et Cosmochimica Acta* **158**, 147–161.

Costa, F., Coogan, L. A. & Chakraborty, S. (2009). The time scales of magma mixing and mingling involving primitive melts and melt-mush interaction at Mid-ocean ridges. *Contributions to Mineral Petrology* DOI 10.1007/s00410–009–0432–3.

Crawford, W. C. & Webb, S. C. (2002). Variation in the distribution of magma in the lower crust and at the Moho beneath the East Pacific Rise at 9°-10°N. *Earth and Planetary Science Letters* **203**, 117–130.

Danyushevsky, L. V., Leslie, R. A. J., Crawford, A. J. & Durance, P. (2004). Melt Inclusions in Primitive Olivine Phenocrysts: the Role of Localized Reaction

Processes in the Origin of Anomalous Compositions. *Journal of Petrology* **45**, 2531–2553.

Danyushevsky, L. V, Perfit, M. R., Eggins, S. M. & Falloon, T. J. (2003). Crustal origin for coupled "ultra depleted" and "plagioclase" signatures in olivine-hosted melt inclusions: evidence from the Siqueiros transform fault, East Pacific Rise. *Contributions to Mineralogy and Petrology* **144**, 619–637.

Defant, M. J. & Nielsen, R. L. (1990). Interpretation of open system petrogenetic processes: phase equilibria constraints on magma evolution. *Geochimica et Cosmochimica Acta* **54**, 87–102.

Detrick, R. S., Buhl, P., Vera, E., Mutter, J., Orcutt, J., Madsen, J. & Brocher, T. (1987). Multi-channel seismic imaging of a crustal magma chamber along the East Pacific Rise. *Nature* **326**, 35–41.

Dosso, S. E., Holland, C. W. & Sambridge, M. (2012). Parallel tempering for strongly nonlinear geoacoustic inversion. *The Journal of the Acoustical Society of America* **132**, 3030–40.

Dosso, S. E. & Wilmut, M. J. (2008). Uncertainty estimation in simultaneous Bayesian tracking and environmental inversion. *The Journal of the Acoustical Society of America* **124**, 82–97.

Dungan, M. A. & Rhodes, J. M. (1978). Residual glasses and melt inclusions in basalts from DSDP Leg 45 and 46: evidence for magma mixing. *Contributions to Mineralogy and Petrology* **67**, 417–431.

Dunn, R. A., Toomey, D. R. & Solomon, S. C. (2000). Three-dimensional seismic structure and physical properites of the crust and shallow mantle beneath the East Pacific Rise at 9°30'N. *Journal of Geophysical Research* **105**, 23,537–23,555.

Earl, D. J. & Deem, M. W. (2005). Parallel Tempering: Theory, Applications, and New Perspectives. *Physical Chemistry Chemical Physics* **7**, 3910–3916.

Falloon, T. F., Green, D. H., Hatton, C. J. & Harris, K. L. (1988). Anhydrous partial melting of a fertile and depleted peridotite from 2 to 30 kb and application to basalt petrogenesis. *Journal of Petrology* **29**, 1257–1282.

France, L., Ildefonse, B. & Koepke, J. (2009). Interactions between magma and hydrothermal system in Oman ophiolite and in IODP Hole 1256D: Fossilization of a dynamic melt lens at fast spreading ridges. *Geochemistry, Geophysics, Geosystems* **10**.

Gale, A., Dalton, C. A., Langmuir, C. H., Su, Y. & Schilling, J. G. (2013). The mean composition of ocean ridge basalts. *Geochemistry, Geophysics, Geosystems* **14**, 489–518.

Gilks, W. R., Richardson, S. & Spiegelhalter, G. J. (1996). *Markov Chain Monte Carlo in Practice*. Chapman and Hall.

Gillis, K. M. & Coogan, L. A. (2002). Anatectic migmatites from the roof of an ocean ridge magma chamber. *Journal of Petrology* **43**, 2075–2095.

Gillis, K. M., Coogan, L. A. & Chaussidon, M. (2003). Volatile behavior in the roof of an axial magma chamber from the East Pacific Rise. *Earth and Planetary Science Letters* **213**, 447–462.

Hekinian, R., Hébert, R., Maury, R. C. & Berger, E. T. (1985). Orthopyroxene-bearing gabbroic xenoliths in basalts from the East Pacific Rise axis near 12°50'N. *Bulletin de Mineralogie* **108**, 691–698.

Hekinian, R. & Walker, R. (1987). Diversity and spatial zonation of volcanic rocks from the East Pacific Rise near 21°N. *Contributions to Mineralogy and Petrology* **96**, 265–280.

Herzberg, C. & O'Hara, M. J. (1998). Phase equilibria constraints on the origin of basalts, picrites, and komatiites. *Earth Science Reviews* **44**, 39–79.

Hirose, K. & Kawamura, K. (1994). A new experimental approach for incremental batch melting of peridotite at 1.5GPa. *Geophysical Research Letters* **21**, 2139–2142.

Hirose, K. & Kushiro, I. (1993). Partial melting of dry peridotite at high pressures: determination of the compositions of melts segregated from peridotite using aggregates of diamond. *Earth and Planetary Science Letters* **114**, 477–489.

Hofmann, A. W. (1988). Chemical differentiation of the Earth: the relationship between mantle, continental crust and oceanic crust. *Earth and Planetary Science Letters* **90**, 297–314.

Hofmann, A. W. (2012). Magma chambers on a slow burner. *Nature* **491**, 677–678.

Huppert, H. E. & Sparks, R. S. J. (1980). The fluid dynamics of a basaltic magma chamber replenished by influx of hot, dense ultrabasic magma. *Contributions to Mineralogy and Petrology* **75**, 279–289.

Jackson, M. G. & Carlson, R. W. (2012). Homogeneous superchondritic Nd-142/Nd-144 in the mid-ocean ridge basalt and ocean island basalt mantle. *Geochemistry, Geophysics, Geosystems* **13**.

Kent, G. M., Harding, A. J. & Orcutt, J. A. (1993). Distribution of magma beneath the East Pacific Rise near the 9°03'N overlapping spreading center from forward modelling of common depth point data. *Journal of Geophysical Research* **98**, 13,913–971,995.

Kirchner, T. M. & Gillis, K. M. (2012). Mineralogical and strontium isotopic record of hydrothermal processes in the lower ocean crust at and near the East Pacific Rise. *Contributions to Mineralogy and Petrology* **164**, 123–141.

Langmuir, C. H. (1989). Geochemical consequences of in situ differentiation. *Nature* **340**, 199–205.

Laubier, M., Gale, A. & Langmuir, C. H. (2012). Melting and Crustal Processes at the FAMOUS Segment (Mid-Atlantic Ridge): New Insights from Olivine-hosted Melt Inclusions from Multiple Samples. *Journal of Petrology* **53**, 665–698.

Liu, L. & Lowell, R. P. (2009). Models of hydrothermal heat output from a convecting, crystallizing, replenished magma chamber beneath an oceanic spreading center. *Journal of Geophysical Research* **114**, doi:10.1029/2008JB005846.

Michael, P. J. & Schilling, J.-G. (1989). Chlorine in mid-ocean ridge magmas: Evidence for assimilation of seawater-influenced components. *Geochimica et Cosmochimica Acta* **53**, 3131–3143.

Minster, J.-F., Minster, B., Treuil, M. & Allegre, C. J. (1977). Systematic use of Trace Elements in Igneous Process Part II: Inverse Problem of the Fractional Crystallisation Processes in Volcanic Suites. *Contributions to Mineralogy and Petrology* **61**, 49–77.

Moore, A., Coogan, L. A., Costa, F. & Perfit, M. R. (2014). Primitive melt replenishment and crystal-mush disaggregation in the weeks preceding the 2005–2006 eruption 9◦50′N, EPR. *Earth and Planetary Science Letters* **403**, 15–26.

Nielsen, R. L., Crum, J., Bourgeois, R., Hascall, K., Forsythe, L. M., Fisk, M. R. & Christie, D. M. (1995). Melt inclusions in high-An plagioclase from the Gorda Ridge: an example of the local diversity of MORB parental magmas. *Contributions to Mineralogy and Petrology* **122**, 34–50.

Nielsen, R. L. & DeLong, S. E. (1992). A numerical approach to boundary layer fractionation: application to differentiation in natural systems. *Contributions to Mineralogy and Petrology* **10**, 355–369.

Niu, Y. & O'Hara, M. J. (2009). MORB mantle hosts the missing Eu (Sr, Nb, Ta and Ti) in the continental crust: New perspectives on crustal growth, crust-mantle differentiation and chemical structure of oceanic upper mantle. *Lithos* **112**, 1–17.

O'Hara, M. J. (1965). Primary magmas and the origin of basalts. *Scotish Journal of Geology* **1**, 19–40.

O'Hara, M. J. (1968a). Are ocean floor basalts primary magmas? *Nature*. **220**, 683–686.

O'Hara, M. J. (1968b). The bearing of phase equilibria studies in synthetic and natural systems on the origin and evolution of basic and ultrabasic rocks. *Earth Science Reviews* **4**, 69–133.

O'Hara, M. J. (1977). Geochemical evolution during fractional crystallization of a periodically refilled magma chamber. *Nature* **266**, 503–507.

O'Hara, M. J. (1978). Thermal history of magmas - low-pressure reference point. *Philosphical Transaction of the Royal Society A - Mathematical Physical and Engineering Sciences* **288**, 627–629.

O'Hara, M. J. (1980). Non-linear nature of the unavoidable long-lived isotopic, trace and major element contamination of a developing magma chamber. *Phiolosophical Tranasactions of the Royal Society Series A - Mathematical Physical and Engineering Sciences* **297**, 215–227.

O'Hara, M. J. & Fry, N. (1996a). The Highly Compatible Trace Element Paradox - Fractional Crystallisation Revisited. *Journal of Petrology* **37**, 859–890.

O'Hara, M. J. & Fry, N. (1996b). Geochemical Effects of Small Packet Crystallisation in Large Magma Chambers - Further resolution of the Highly Compatible Element Paradox. *Journal of Petrology* **37**, 891–925.

O'Hara, M. J. & Herzberg, C. (2002). Interpretation of trace element and isotope features of basalts: Relevance of field relations, petrology, major element data, phase equilibria, and magma chamber modeling in basalt petrogenesis. *Geochimica et Cosmochimica Acta* **66**, 2167–2191.

O'Neill, H. S. C. & Jenner, F. E. (2012). The global pattern of trace-element distributions in ocean floor basalts. *Nature* **491**, 698+.

Pan, Y. & Batiza, R. (2002). Mid-ocean ridge magma chamber processes: constraints from olivine zonation in lavas from the East Pacific Rise at 9°30'N and 10°30'N. *Journal of Geophysical Research* **107**.

Perfit, M. R., Fornari, D. J., Malahoff, A. & Embley, R. W. (1983). Geochemical Studies of Abyssal Lavas Recovered by DSRV Alvin From Eastern Galapagos Rift, Inca

Transform, and Ecuador Rift 3: Trace element abundnces and petrogenesis. *Journal of Geophysical Research* **88**, 10551–10572.

Perfit, M. R., Fornari, D. J., Smith, M. C., Bender, J. F., Langmuir, C. H. & Haymon, R. M. (1994). Small scale spatial and temporal variations in mid-ocean ridge crest magmatic processes. *Geology* **22**, 375–379.

Perfit, M. R., Wanless, V. D., Ridley, W. I., Klein, E. M., Smith, M. C., Goss, A. R., Hinds, J. S., Kutza, S. W. & Fornari, D. J. (2012). Lava Geochemistry as a Probe into Crustal Formation at the East Pacific Rise. *Oceanography* **25**, 89–93.

Pollock, M. A., Klein, E. M., Karson, J. A. & Coleman, D. S. (2009). Compositions of dikes and lavas from the Pito Deep Rift: Implications for crustal accretion at superfast spreading centers. *Journal of Geophysical Research* **114**.

Presnall, D. C. & Hoover, J. D. (1987). High pressure phase equilibrium constraints on the origin of mid-ocean ridge basalt. In: Mysen, B. O. (ed.) *Magmatic Processes: Physicochemical principles*. The Geochemical Society, 75–90.

Rhodes, J. M., Dungan, M. A., Blanchard, D. P. & Long, P. E. (1979). Magma mixing at mid-ocean ridges: evidence from basalts drilled near 22°N on the Mid-Atlantic Ridge. *Tectonophysics* **55**, 35–61.

Ridley, I., Perfit, M. R., Smith, M. C. & Fornari, D. J. (2006). Magmatic processes in developing oceanic crust revealed in a cumulate xenolith collected at the East Pacific Rise, 9°50'N. *Geochemistry Geophysics Geosystems* **7**, doi: 10.1029/2006GC001316.

Roeder, P., Gofton, E. & Thornber, C. (2006). Cotectic proportions of olivine and spinel in olivine-tholeiitic basalt and evaluation of pre-eruptive processes. *Journal of Petrology* **47**, 883–900.

Salters, V. J. M. & Stracke, A. (2004). Composition of the depleted mantle. *Geochemistry Geophysics Geosystems* **5**, doi:10.1029/2003GC000597.

Shorttle, O. (2015). Geochemical variability in MORB controlled by concurrent mixing and crystallisation. *Earth and Planetary Science Letters* **424**, 1–14.

Sobolev, A. V & Shimizu, N. (1993). Ultra-depleted primary melt inclusions in an olivine from the Mid-Atlantic Ridge. *Nature* **363**, 151–154.

Stewart, M. A., Klein, E. M. & Karson, J. A. (2002). Geochemistry of dikes and lavas from the north wall of th Hess Deep Rift: insights into the four-dimensional character of crustal construction at fast spreading mid-ocean ridges. *Journal of Geophysical Research* **107**, DOI 10.1029/2001JB000545.

Stewart, M. A., Klein, E. M. & Karson, J. A. (2003). Geochemical relationships between dikes and lavas at the Hess Deep Rift: Implications for magma eruptibility. *Journal of Geophysical Research* **108**, doi:10.1029/2001JB001622.

Stolper, E. (1980). A Phase Diagram for Mid-Ocean Ridge Basalts: Preliminary Results and Implications for Petrogenesis. *Contributions to Mineralogy and Petrology* **74**, 13–27.

Sun, S. -s. & McDonough, W. F. (1989). Chemical and isotopic systematics of oceanic basalts: implications for mantle composition and processes. In: Saunders, A. D. & Norry, M. J. (eds) *Magmatism in the ocean basins*. Geological Society of London Special Publication, 313–345.

Workman, R. K. & Hart, S. R. (2005). Major and trace element composition of the depleted MORB mantle (DMM). *Earth and Planetary Science Letters* **231**, 53–72.

FIGURE CAPTIONS

Figure 1. Basalt major element compositions projected from diopside and $Na_2O{\cdot}Si_3O_6$ and $K_2O{\cdot}Si_3O_6$ onto the forsterite-anorthite-quartz plane using the empirical projection scheme of Herzberg and O'Hara (1998; see their Fig. 2) colour coded by Mg# (calculated here as $Mg/[Mg+Fe_{total}]$; atomic): (a) experimentally produced MORB-like melts saturated with upper mantle phases (olivine, orthopyroxene ± clinopyroxene ± spinel) at various pressures (P: Stolper, 1980; Falloon and Green, 1988; Falloon et al., 1988; Hirose and Kushiro, 1993; Hirose and Kawamura, 1994) and troctolitic (T; black rims) and gabbroic (G; purple rims) assemblage at 1 atmosphere (Bartels et al., 1991; Bender et al., 1978; Grove et al., 1982; Grove and Bryan, 1983; Juster et al., 1989; Kohut and Nielsen, 2003; Tormey et al., 1987; Thy et al., 2004; Yang et al., 1996). Blue (8-12 kbar), green (15 kbar) and red (18-20 kbar) rims on the peridotite melt compositions show the progressive displacement of melts towards olivine, and higher Mg#, with increasing pressure. Experimental melt compositions with >0.5 wt% K_2O or > 6 wt% Na_2O were excluded; (b) 4041 normal MORB glasses ($K_2O/TiO_2 \leq 0.15$) from the EPR (Melson et al., 2002) generally overlap the field of troctolite and gabbro assemblage saturated experimental melts at 1 atmosphere and are substantially displaced from high-pressure melts saturated with olivine and orthopyroxene. The differentiation of these MORB is shown by the decreasing Mg# away from the Fo-An tie line and towards SiO_2 and is

largely similar to that in the experimental runs (cf. Stolper, 1980); (c) MORB from Hess Deep (Stewart et al., 2002); (d) MORB from Pito Deep (Pollock et al., 2009); (e) MORB from 9°N on the EPR (Perfit et al., 2012).

Figure 2. Cartoon model (not to scale) and flow diagram explaining the differentiation model assumed herein – see text for discussion. R = replenishment; T = tapping; M = mixing and mush zone disaggregation allowing interstitial melt back into the eruptible reservoir; A = assimilation. PFC = perfect fractional crystallization; PEC = perfect equilibrium crystallization.

Figure 3. Examples of synthetic melt composition datasets shown as MgO versus Th normalized to the parental melt Th content (Figure 4 shows the same models for MgO versus Cr). Part a shows the colour scale based on the Nb/Y of the melt. The parental melt composition is the same in all parts and a fractional crystallization model starting from this is shown as the green line. Model parameters used are as on figure or if not listed on the figure as in brackets: Erupt = % of mixed magma erupted (4±1%); F_{AML} = % of melt remaining in AML after crystallization; Replenishment = average % mass of chamber replenished per cycle; Boundary layer = % of melt partitioned into the boundary layer before crystallization (remainder left in the AML; 50±10%); F_{BL} = % of melt remaining in boundary after crystallization (85±10%); $F_{returned}$ = % of interstitial melt returned from the boundary layer after crystallization (92.5±5%). Constant parameters are: mass fraction of AML assimilated per cycle: 0.25±0.01%. Fraction troctolite

crystallization prior to mixing replenishing melt into magma reservoir: 2.5±5%. See text for discussion.

Figure 4. As figure 3 only showing model results for Cr as a function of MgO. The parental melt composition is the same in all parts.

Figure 5. Example of how the summary statistics used in the inversion represent the dataset. The average and standard deviation of an elements abundance is calculated for all data within a given 0.5 wt% MgO bin and the proportion of the data that fall in each bin is determined (inset).

Figure 6. Geochemical characteristics of the three basalt suites modeled here: (a) distribution of MgO contents in 0.5 wt% MgO bins; (b) covariation of Cr with MgO with the solid lines running through the average value in 0.5 wt% bins (inset shows the relative standard deviation of the Cr content in 0.5 wt% MgO bins); (c) covariation of Nb with MgO with the solid lines running through the average value in 0.5 wt% bins (inset shows the relative standard deviation of the Nb content in 0.5 wt% MgO bins) and a fractional crystallization model (green line) using the most primitive composition as the starting composition.

Fig. 7. Probability distributions for the mean values (a-h), and their standard deviations (i-p), of the controlling input model parameter (Table 1). The mass fraction of replenishing melt (g) is relative to average mass of the chamber immediate prior to

eruption. The value of each parameter used in each model iteration (i.e. a replenish-mix-erupt-crystallize cycle) is drawn from the probability distribution defined by these averages and standard deviations. Because only physically meaningful values are allowed (Table 1), the average value of the parameter used does not have to match the average of the probability distribution it is drawn from.

Fig. 8. Probability distributions for the parental melt compositions for the three study sites with the MAP solutions shown as dashed lines. All concentrations in ppm except where noted.

Fig. 9. Primitive mantle (Sun and McDonough, 1989) normalized spidergram showing possible parental N-MORB compositions. Standard models (grey) that have been used in chemodynamic modeling are substantially less depleted in incompatible elements than: (i) the parental melt compositions determined in this study (MAP solutions are shown here; see Fig 8 for the probability distribution of parental melt compositions); (ii) the most primitive EPR MORB; and (iii) the parental MORB estimate of Niu and O'Hara (2009).

Figure 10. Variations in the plagiophile elements in the N-MORB sample suites studied here. Column 1: Hess Deep; Column 2: Pito Deep; Column 3: 9°N. Note the different scales on parts k and n relative to the comparable figures. (a-c) MgO versus Sr showing the natural datasets have much greater variability in Sr than predicted by the forward model (blue symbols) (d-f) MgO versus Pr colour coded by the samples Sr content; (g-i)

Sr versus Pr; (j-l) Ba versus Sr colour coded by the samples MgO content; and (m-o) Nb versus Ba. See text for discussion.

Fig. 11. Covariation of FeO (a-d) and Al_2O_3 (e-h) with MgO in samples from Hess Deep, Pito Deep, 9°N and an EPR MORB compilation (Gale et al., 2013) colour coded by the samples Ba content. Note that parts d and h are colour coded by Ln[Ba] to allow the much larger variability in Ba in this dataset than the others to be observed clearly. In all cases except the 9°N data the high Ba samples have a strong tendency toward high Al and low Fe at a given MgO content.

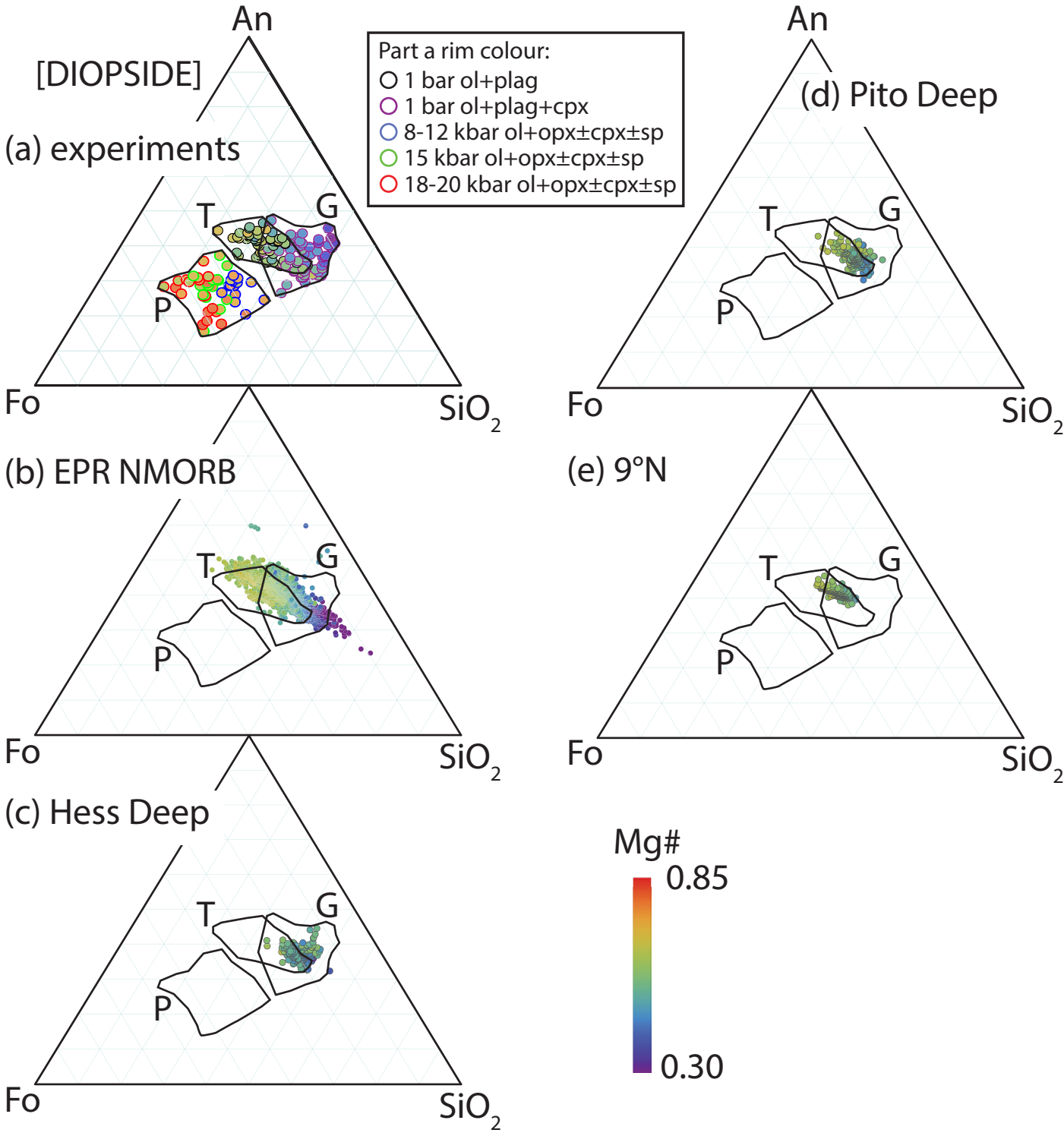
[DIOPSIDE]
(a) experiments
(b) EPR NMORB
(c) Hess Deep
(d) Pito Deep
(e) 9°N
Part a rim colour:
1 bar ol+plag
1 bar ol+plag+cpx
8-12 kbar ol+opx±cpx±sp
15 kbar ol+opx±cpx±sp
18-20 kbar ol+opx±cpx±sp
An
Fo
SiO2
T
G
P
Mg#
0.85
0.30

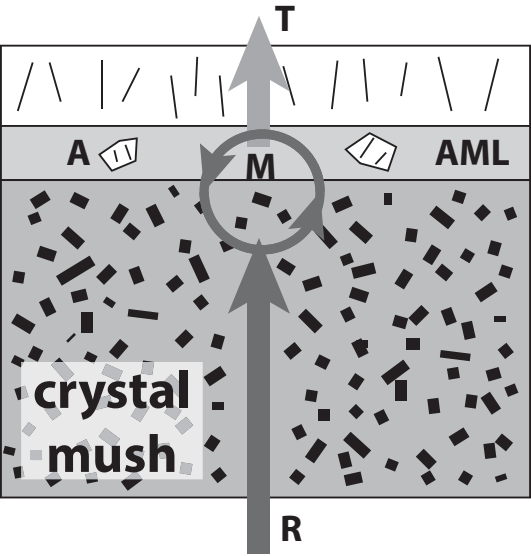
T
A
M
AML
crystal
mush
R

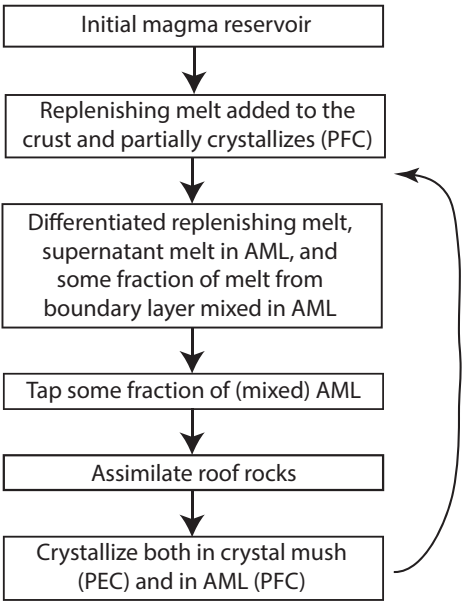
Initial magma reservoir
Replenishing melt added to the crust and partially crystallizes (PFC)
Differentiated replenishing melt, supernatant melt in AML, and some fraction of melt from boundary layer mixed in AML
Tap some fraction of (mixed) AML
Assimilate roof rocks
Crystallize both in crystal mush (PEC) and in AML (PFC)

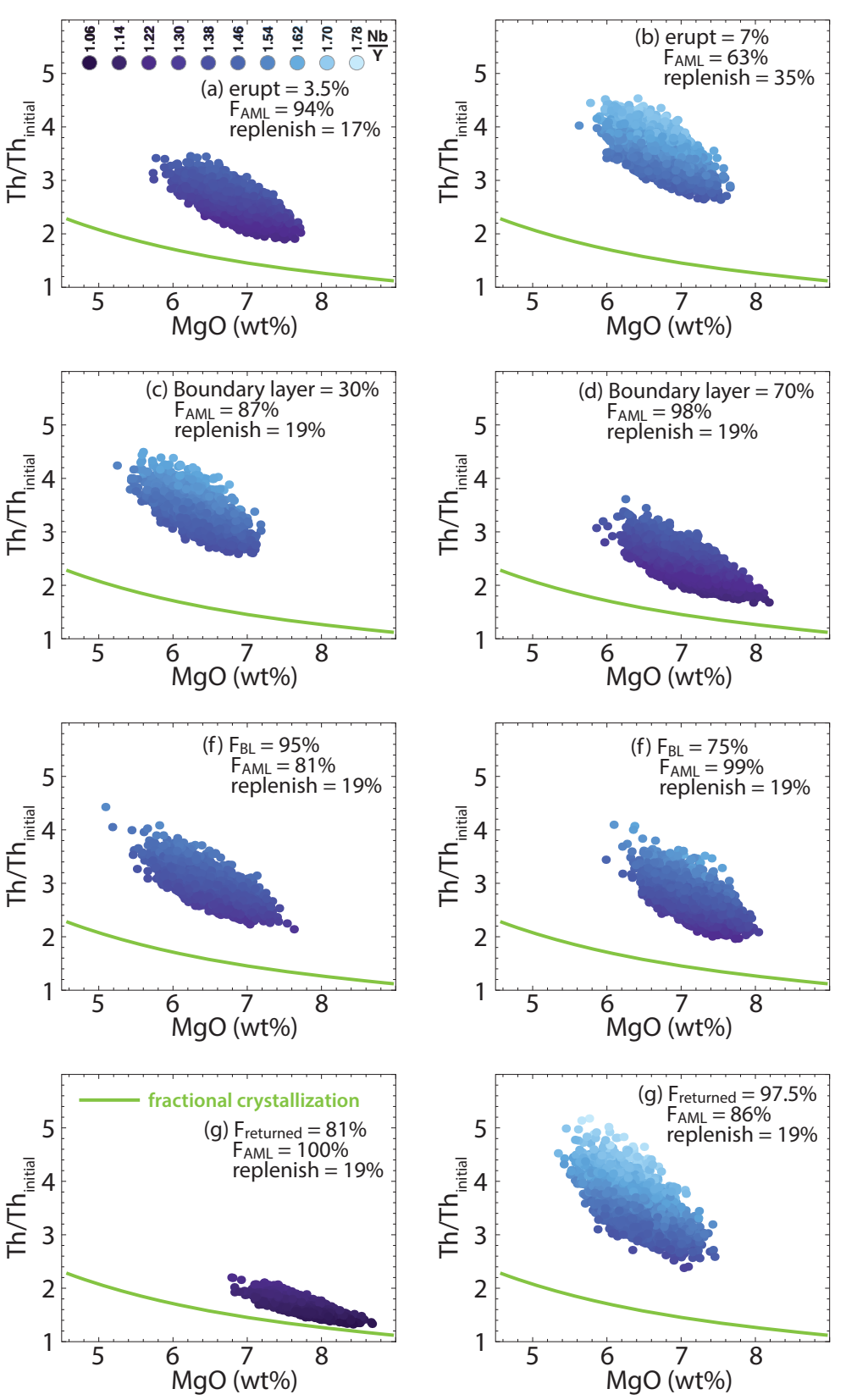
1.06
1.14
1.22
1.30
1.38
1.46
1.54
1.62
1.70
1.78
Nb/Y
(a) erupt = 3.5%
F_AML = 94%
replenish = 17%
(b) erupt = 7%
F_AML = 63%
replenish = 35%
(c) Boundary layer = 30%
F_AML = 87%
replenish = 19%
(d) Boundary layer = 70%
F_AML = 98%
replenish = 19%
(f) F_BL = 95%
F_AML = 81%
replenish = 19%
(f) F_BL = 75%
F_AML = 99%
replenish = 19%
fractional crystallization
(g) F_returned = 81%
F_AML = 100%
replenish = 19%
(g) F_returned = 97.5%
F_AML = 86%
replenish = 19%
Th/Th_initial
MgO (wt%)

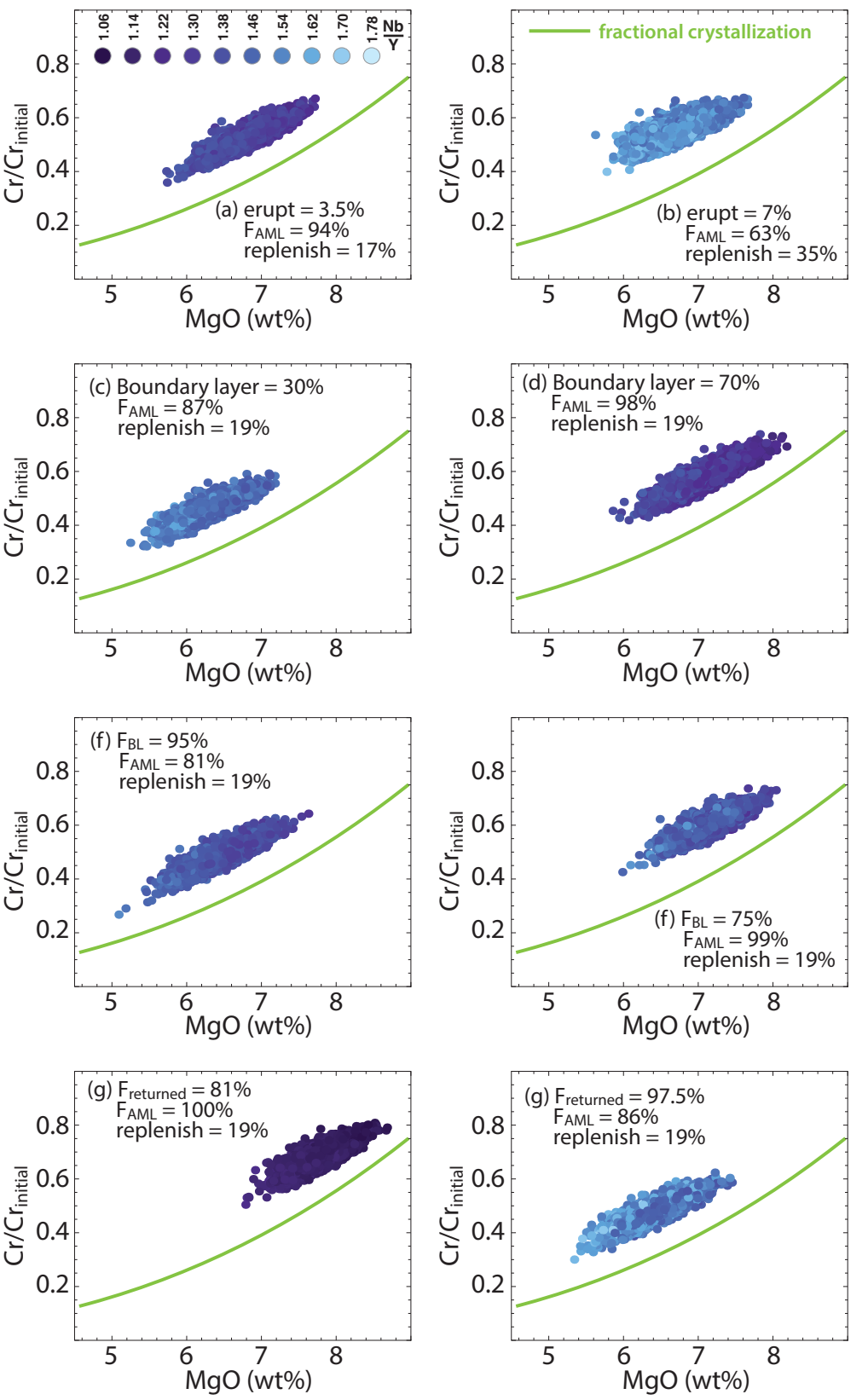
1.06
1.14
1.22
1.30
1.38
1.46
1.54
1.62
1.70
1.78
Nb/Y
fractional crystallization
(a) erupt = 3.5%
FAML = 94%
replenish = 17%
(b) erupt = 7%
FAML = 63%
replenish = 35%
(c) Boundary layer = 30%
FAML = 87%
replenish = 19%
(d) Boundary layer = 70%
FAML = 98%
replenish = 19%
(f) FBL = 95%
FAML = 81%
replenish = 19%
(f) FBL = 75%
FAML = 99%
replenish = 19%
(g) Freturned = 81%
FAML = 100%
replenish = 19%
(g) Freturned = 97.5%
FAML = 86%
replenish = 19%
Cr/Crinitial
MgO (wt%)

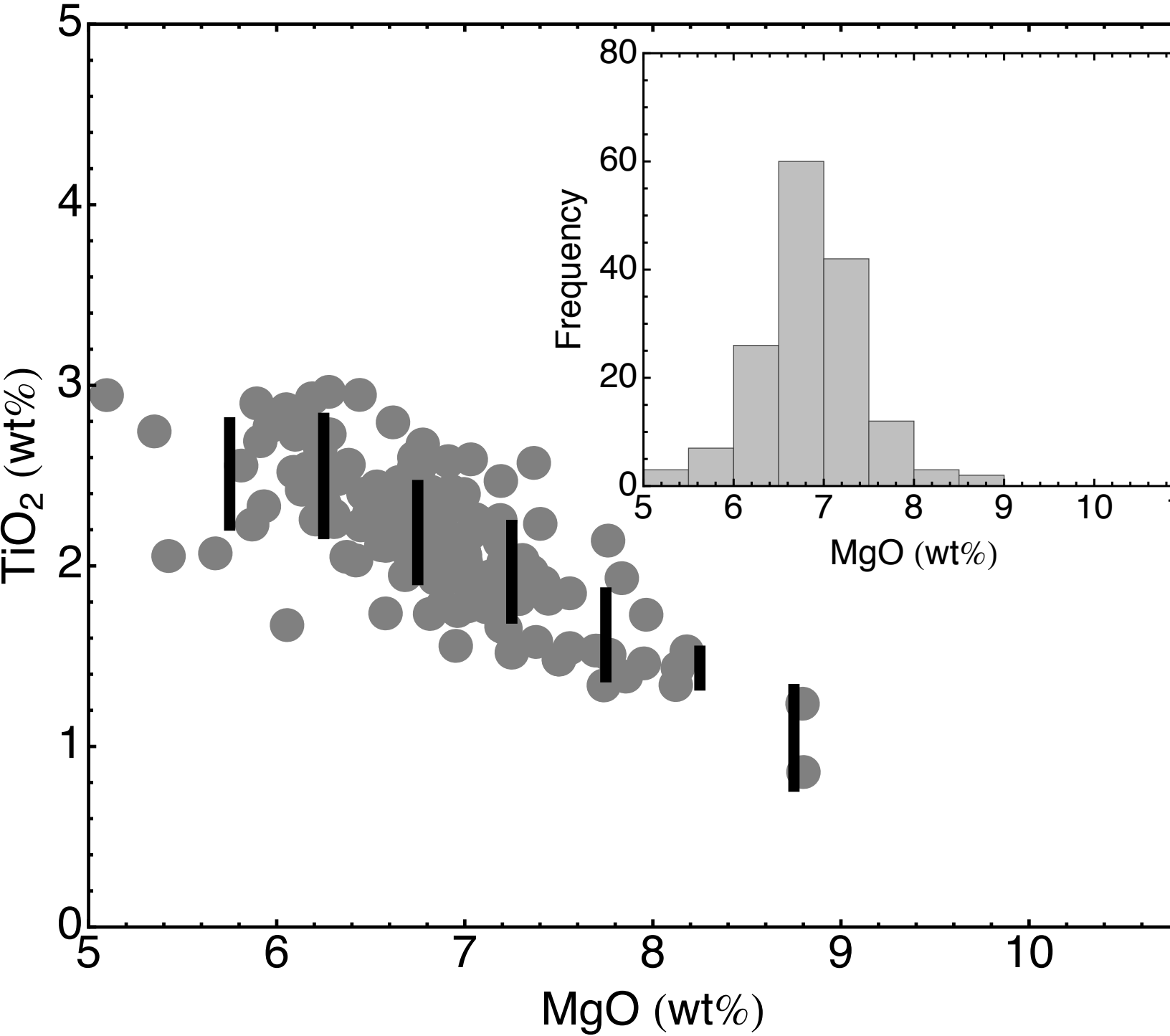
TiO2 (wt%)
MgO (wt%)
Frequency
MgO (wt%)

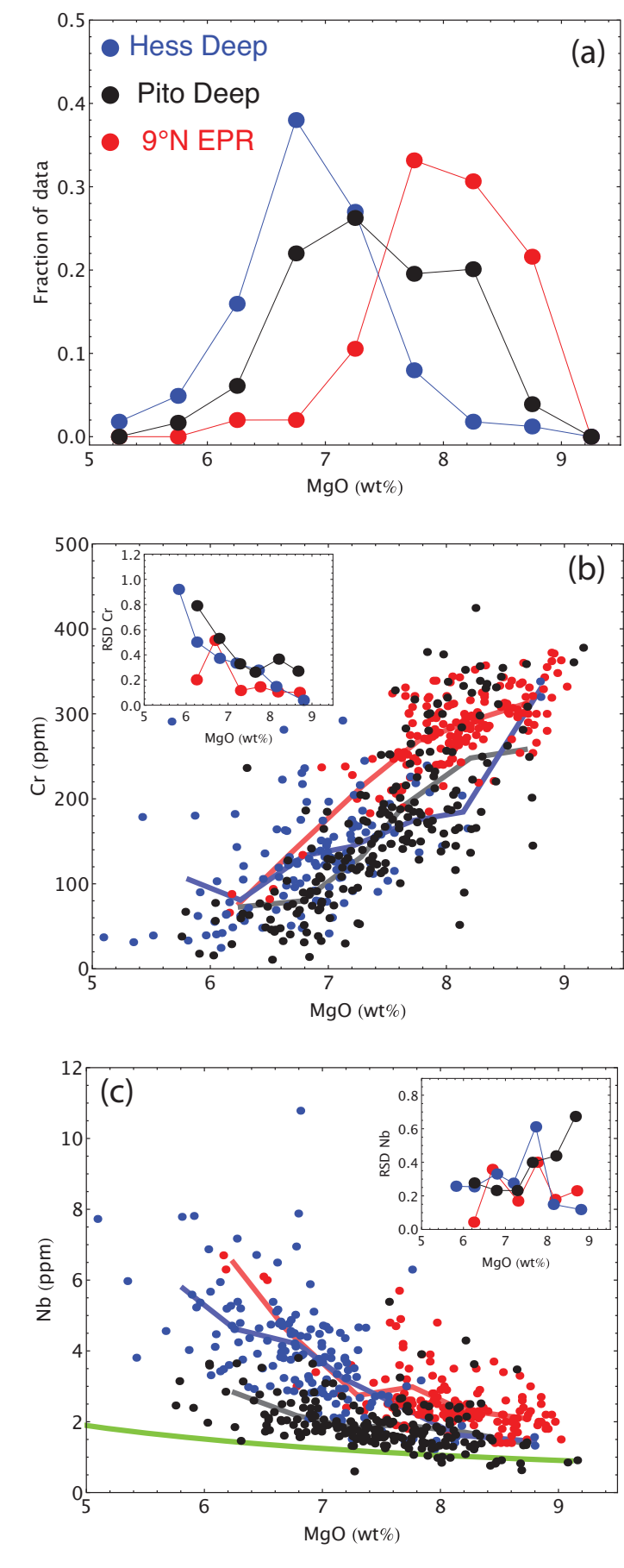
(a)
Hess Deep
Pito Deep
9°N EPR
Fraction of data
MgO (wt%)
(b)
Cr (ppm)
MgO (wt%)
RSD Cr
MgO (wt%)
(c)
Nb (ppm)
MgO (wt%)
RSD Nb
MgO (wt%)

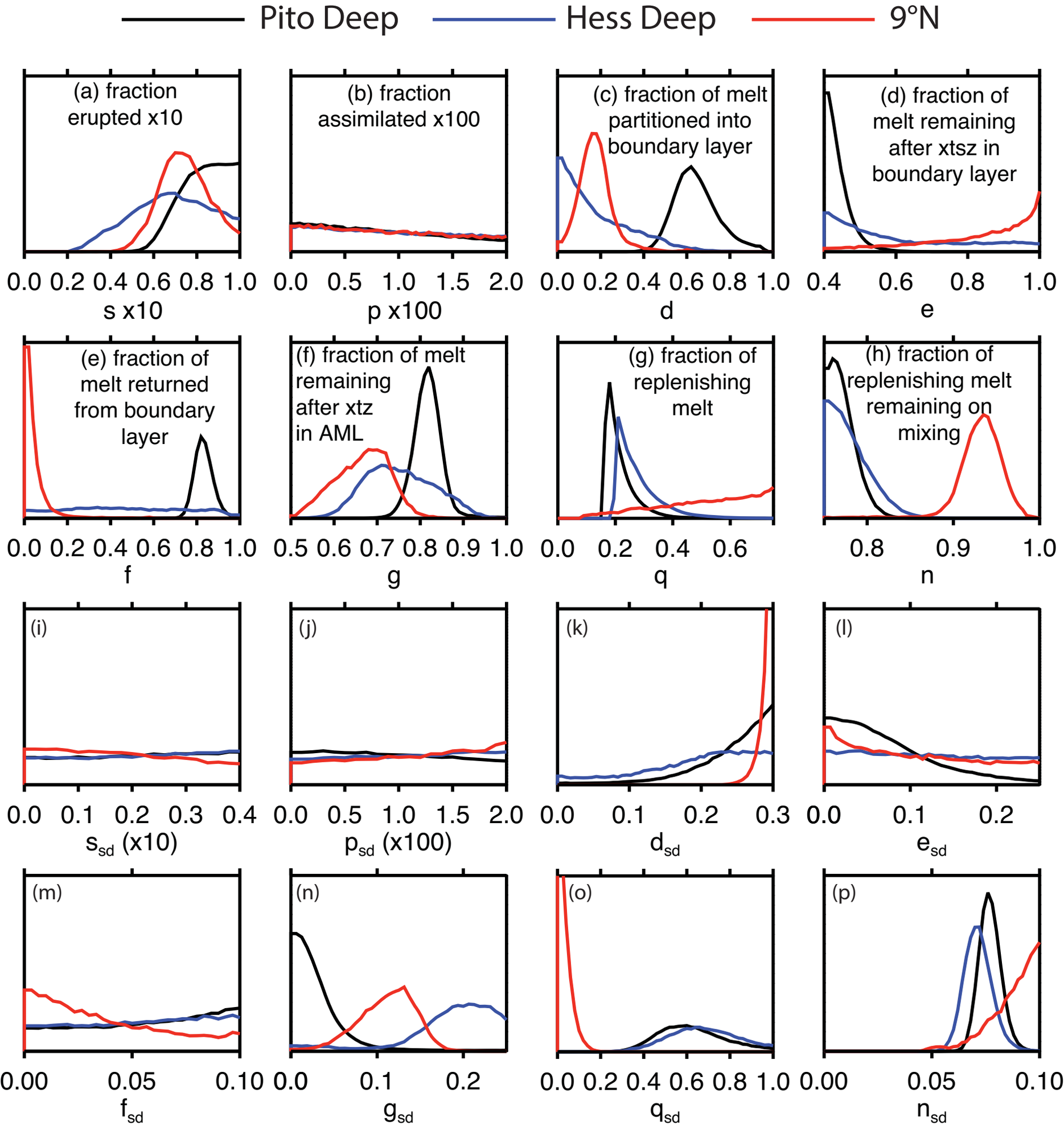
Pito Deep
Hess Deep
9°N
(a) fraction erupted x10
s x10
(b) fraction assimilated x100
p x100
(c) fraction of melt partitioned into boundary layer
d
(d) fraction of melt remaining after xtsz in boundary layer
e
(e) fraction of melt returned from boundary layer
f
(f) fraction of melt remaining after xtz in AML
g
(g) fraction of replenishing melt
q
(h) fraction of replenishing melt remaining on mixing
n
(i)
s_{sd} (x10)
(j)
p_{sd} (x100)
(k)
d_{sd}
(l)
e_{sd}
(m)
f_{sd}
(n)
g_{sd}
(o)
q_{sd}
(p)
n_{sd}

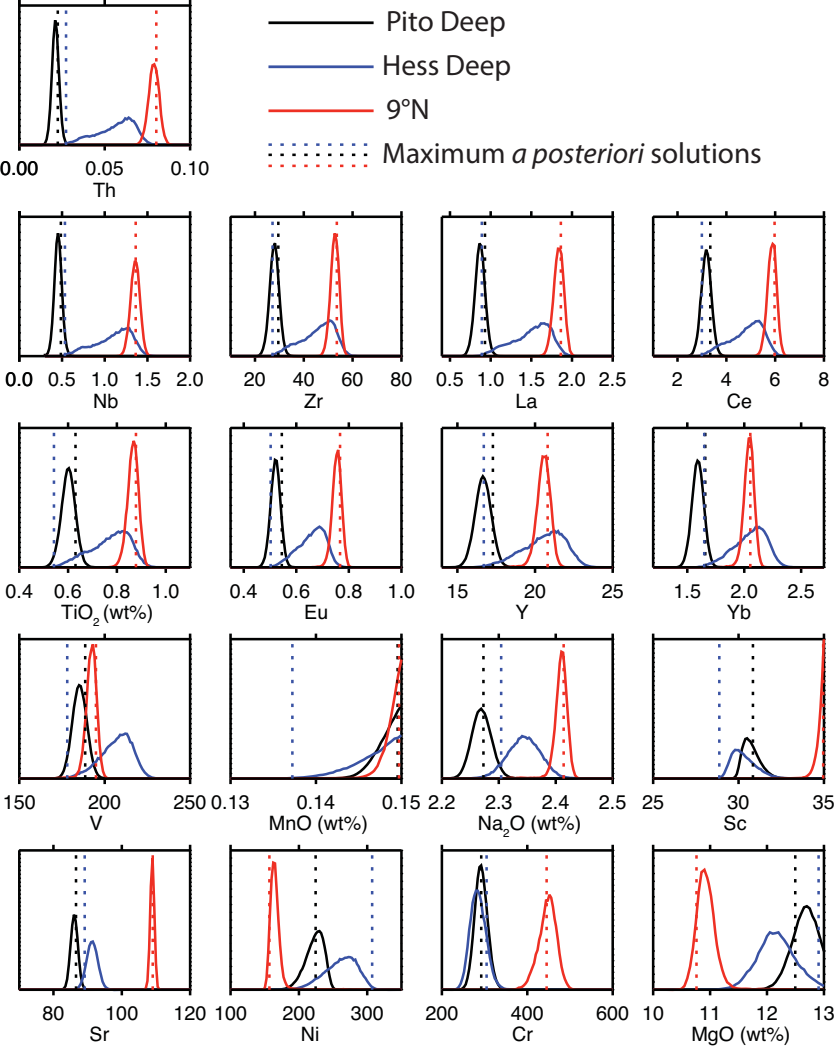
Pito Deep
Hess Deep
9°N
Maximum *a posteriori* solutions
0.00 0.05 0.10
Th
0.0 0.5 1.0 1.5 2.0
Nb
20 40 60 80
Zr
0.5 1.0 1.5 2.0 2.5
La
2 4 6 8
Ce
0.4 0.6 0.8 1.0
TiO_2 (wt%)
0.4 0.6 0.8 1.0
Eu
15 20 25
Y
1.5 2.0 2.5
Yb
150 200 250
V
0.13 0.14 0.15
MnO (wt%)
2.2 2.3 2.4 2.5
Na_2O (wt%)
25 30 35
Sc
80 100 120
Sr
100 200 300
Ni
200 400 600
Cr
10 11 12 13
MgO (wt%)

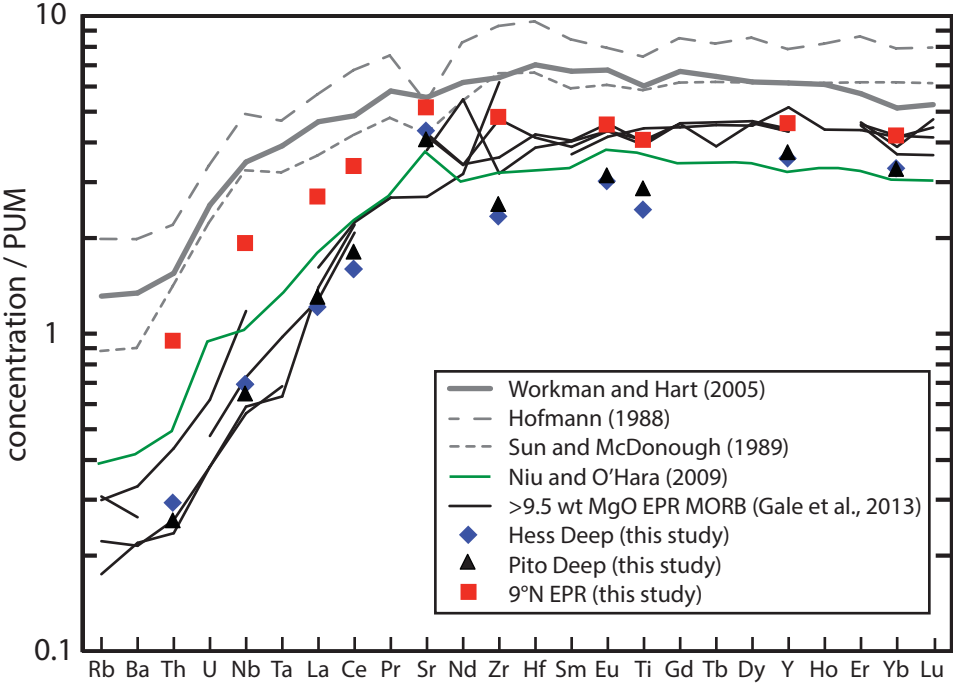
10
1
0.1
concentration / PUM
Rb Ba Th U Nb Ta La Ce Pr Sr Nd Zr Hf Sm Eu Ti Gd Tb Dy Y Ho Er Yb Lu
Workman and Hart (2005)
Hofmann (1988)
Sun and McDonough (1989)
Niu and O'Hara (2009)
>9.5 wt MgO EPR MORB (Gale et al., 2013)
Hess Deep (this study)
Pito Deep (this study)
9°N EPR (this study)

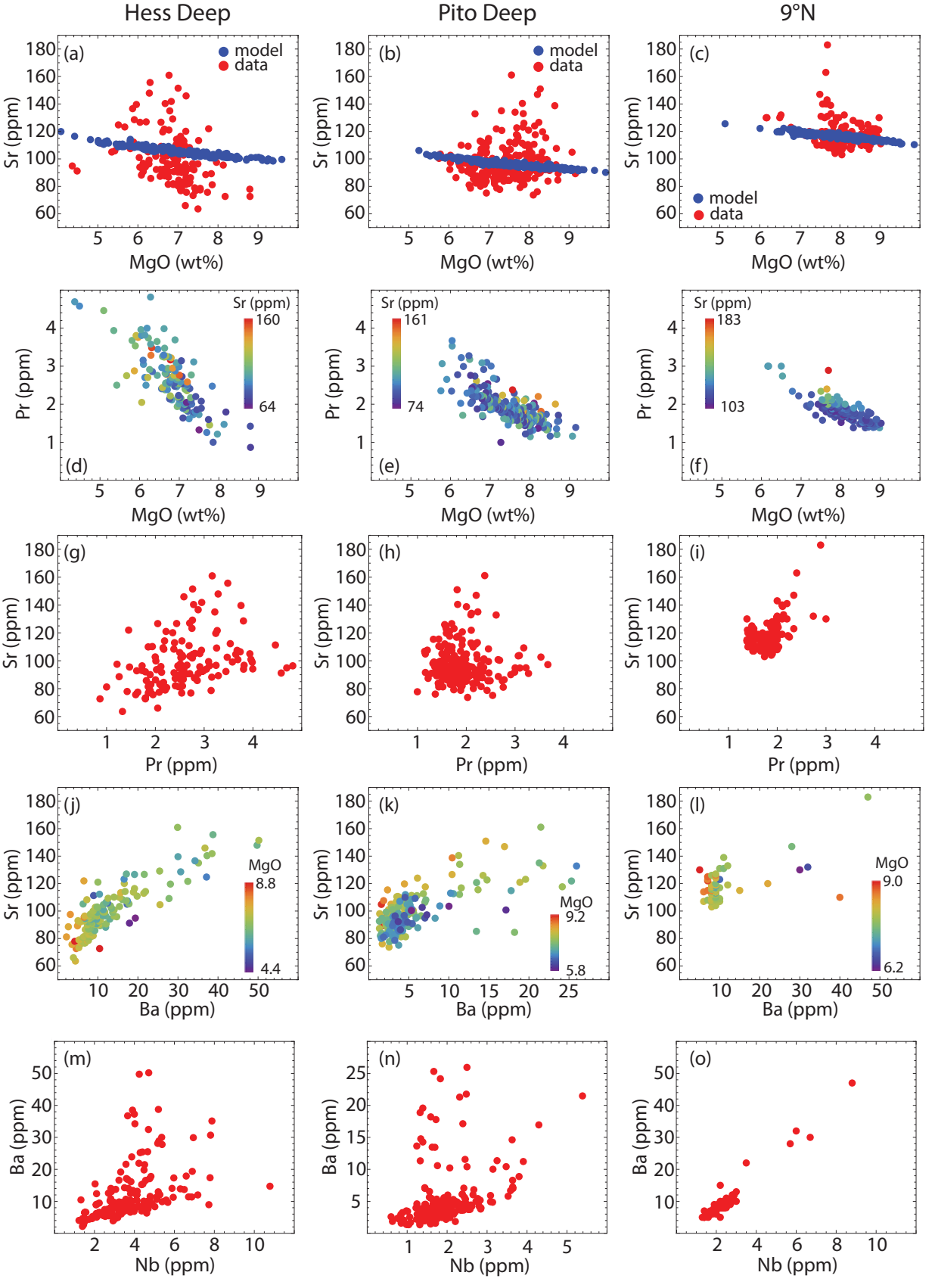
Hess Deep
Pito Deep
9°N
(a)
(b)
(c)
model
data
Sr (ppm)
MgO (wt%)
(d)
(e)
(f)
Sr (ppm)
160
64
161
74
183
103
Pr (ppm)
(g)
(h)
(i)
Pr (ppm)
(j)
(k)
(l)
MgO
8.8
4.4
9.2
5.8
9.0
6.2
Ba (ppm)
(m)
(n)
(o)
Nb (ppm)

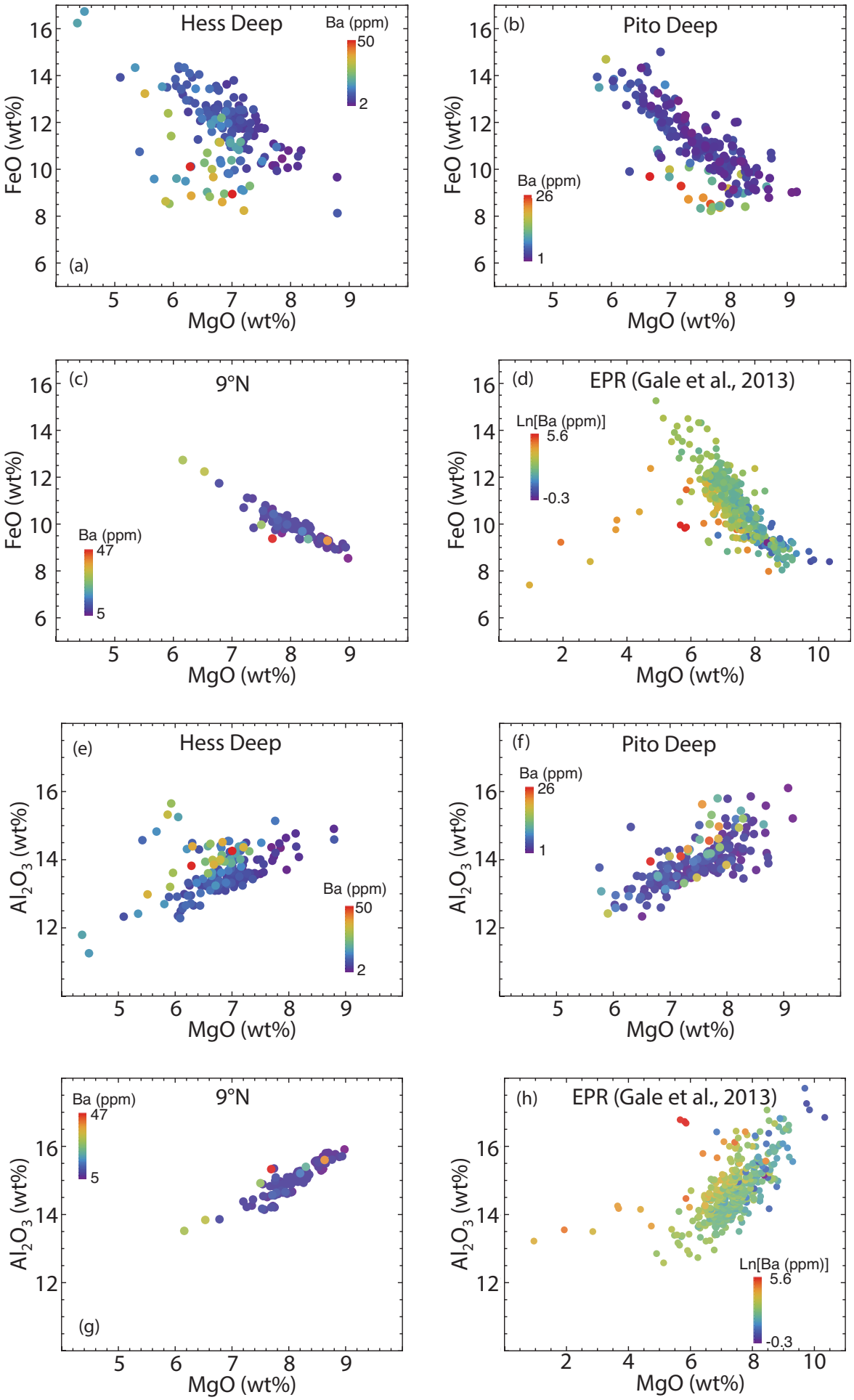
(a)
Hess Deep
Ba (ppm)
50
2
FeO (wt%)
MgO (wt%)
(b)
Pito Deep
Ba (ppm)
26
1
FeO (wt%)
MgO (wt%)
(c)
9°N
Ba (ppm)
47
5
FeO (wt%)
MgO (wt%)
(d)
EPR (Gale et al., 2013)
Ln[Ba (ppm)]
5.6
-0.3
FeO (wt%)
MgO (wt%)
(e)
Hess Deep
Ba (ppm)
50
2
Al2O3 (wt%)
MgO (wt%)
(f)
Pito Deep
Ba (ppm)
26
1
Al2O3 (wt%)
MgO (wt%)
(g)
9°N
Ba (ppm)
47
5
Al2O3 (wt%)
MgO (wt%)
(h)
EPR (Gale et al., 2013)
Ln[Ba (ppm)]
5.6
-0.3
Al2O3 (wt%)
MgO (wt%)